# Preparation of Carbon Supported Single Pd, Pt and Bimetallic Pd-Pt Nanoparticles Using Supercritical $CO_2$ Deposition

**by**

**Betül Cangül**

**A Thesis Submitted to the**
**Graduate School of Sciences & Engineering**
**in Partial Fulfillment of the Requirements for**
**the Degree of**

**Master of Science**
**in**
**Materials Science & Engineering**

**Koc University**

**February 2009**

Koc University

Graduate School of Sciences and Engineering

This is to certify that I have examined this copy of a master's thesis by

Betül Cangül

and have found that it is complete and satisfactory in all respects,
and that any and all revisions required by the final
examining committee have been made.

Committee Members:

Can Erkey, Ph. D. (Advisor)

Metin Türkay, Ph. D.

Mehmet Somer, Ph. D.

Date: 16.02.2009

**ABSTRACT**

Metal nanoparticles supported on high surface area carbon substrates are used extensively as catalysts for a wide variety of reactions. Among these catalysts, carbon supported single Pd and bimetallic Pd-Pt catalysts are commonly used for hydrogenation reactions in the fine chemical industry. In order to prepare carbon supported catalysts, the supercritical fluid deposition technique has recently been receiving increased attention. This process involves the dissolution of an organometallic precursor (OM) in a supercritical fluid and the exposure of the carbon support to the solution. After adsorption of the precursor onto the support, the metallic precursor is converted to its metal form by chemical or thermal reduction. Although many studies have been conducted in order to prepare supported single metallic nanoparticles so far; there are very few studies regarding the preparation of supported bimetallic nanoparticles by $scCO_2$ deposition in the literature.

In this thesis the preparation of carbon black (Black Pearl 2000) supported single Pd and Pt nanoparticles by supercritical $CO_2$ deposition was investigated. The $scCO_2$ depostion was utilized also for the preparation of carbon supported bimetallic Pt-Pd by introduing two different deposition alternatives consisting of the preparation starting from the formation of carbon supported platinum (Pt/C) followed by deposition of Pd precursor and reduction; and the simultaneous adsorption and subsequent reduction of the precursors. Palladium (II) acetylacetonate ($Pd(acac)_2$) and dimethyl (cyclooctadiene) platinum (II) ($PtMe_2COD$) were utilized as metallic precursors. The adsorption isotherms of $Pd(acac)_2$ and $PtMe_2COD$ on BP2000 in $scCO_2$ at the experimental conditions; 20 MPa and 60 $^0$C was determined in order to understand the correlation between the concentration of the OMs in the supercritical phase and the uptake amount of the OMs on the substrate at the given experimental conditions. A mass transfer model was found to represent the experimental data on the kinetics of adsorption of $Pd(acac)_2$ onto BP2000 in $scCO_2$ fairly

well with a fitting error of 5.6 %. With the help of the model obtained, the effect or process parameters like the tortuosity and particle size of support and isotherm constants on the adsorption kinetics was investigated. In order to reduce the OMs adsorbed on the substrate, chemical reduction with $H_2$ in $scCO_2$ was utilized. Increasing reduction temperature and metal loading caused an increase in Pd particle size. From the TEM image, it was seen that the Pd particles were irregularly distributed and the size range of the particles was 3-100 nm, whereas Pt nanoparticles were homogeneously distributed with a size range of 2-4 nm. From the TEM image of the supported bimetallic Pt-Pd nanoparticles, it was found that addition of Pt increased the homogeneity and reduced the particle size on the support compared to single Pd nanoparticles. From the EDS results, it was seen that there was a heterogeneous mixture of the bimetallic nanoparticles. Pt-rich nanoparticles had diameters of between 3-5 nm, whereas Pd-rich nanoparticles were larger with diameters of around 10 nm.

**Keywords:** supercritical deposition, carbon, nanoparticles, platinum, palladium, organometallic.

**ÖZET**

Yüksek yüzey alanlı karbon destekli metal nanoparçacıklar yaygın olarak çok çeşitli reaksiyonlarda katalizör olarak kullanılmaktadır. Bu katalizörler arasında karbon destekli tek metalli paladyum (Pd) ve iki metalli paladyum-platinyum (Pd-Pt) katalizörleri sık olarak kimya endüstrisinde hidrojenasyon reaksiyonlarında kullanılmaktadır. Son yıllarda bu tip katalizörlerin hazırlanmasında süperkritik akışkan depozisyon prosesi artan bir ilgi görmektedir. Bu proses metal sağlayıcılarının superkritik akışkan içerisinde çözülmesi ve karbon desteğin bu solusyona maruz kalmasını gerektirmektedir. Metal sağlayıcının destek üzerine adzorbsiyonundan sonra, organonmetalik yapı kimyasal veya ısısal indirgenmeyle metal formuna dönüştürülür.

Bu tezde karbon siyahı (Black Pearl 2000 (BP 2000)) destekli tek metalli Pd ve Pt parçacıklarının süperkritik depozisyon yöntemi kullanılarak hazırlanması araştırılmıştır. Bu yöntem ayrıca karbon destekli iki metalli Pd-Pt nanoparçacıklarının da iki farklı alternatif depozisyon metoduyla hazırlanmasında kullanılmıştır. Bu metodlardan ilki, oncelikle Pt/C katalizörünü hazırlama, bunun üzerine Pd metal sağlayıcının adzorbe olmasını sağlama ve metal sağlayıcıyı indirgeme aşamalarından oluşmaktadır. İkinci metod ise hem Pd hem de Pt metal sağlayıcılarının aynı anda karbon üzerine adsorbe olup, yine eş zamanlı indirgenmelerinden oluşmaktadır. Metal sağlayıcılar olarak Paladyum (II) asetilasetonat ($Pd(acac)_2$) ve dimetil siklooktadiyen platinyum (II) ($PtMe_2COD$) kullanılmıştır. Süperkritik depozisyonun önemli bir aşaması olan metal sağlayıcıların destek üzerine adsorpsiyonunu anlayabilmek için $Pd(acac)_2$ ve 'nin deneysel şartlarda; 20 MPa ve 60 $^0$C'deki adsorpsiyon izotermleri elde edilmiştir. Yine bu sıcaklık ve basınç değerlerinde $Pd(acac)_2$'nin BP 2000 üzerine adsorpsiyon kinetiğini deneysel datayı sadece 5.6% uyma hatası vererek temsil edebilen bir kütle transfer modeli geliştirişmiştir. Bu geliştirilen model sayesinde desteğin tortuozitesi, partikül büyüklüğü ve izoterm sabitlerinin

adsorpsiyon kinetiğine olan etkilerini incelemek mümkün olmuştur. Karbon destek üzerine adsorplanan metal sağlayıcıları indirgemek için süperkritik karbon dioksit içerisinde hidrojenle kimyasal indirgenme yapılmıştır. İndirgenme sıcaklığını ve metal yüklemesini arttırmak Pd partikül büyüklüğünü arttırmıştır. Hazırlanan katalizörlerin TEM sonuçlarından Pd'un karbon destek üzerinde büyüklüğü 3-100 nm arasında değişen parçacıklar halinde düzensiz bir biçimde yayılmış olduğu görülürken Pt'un büyüklüğü 2-4 nm arasında olup, destek üzerinde homojen bir dağılım göstermiştir. Karbon destekli iki metalli Pt-Pd katalizörlerinin TEM resimlerinde ise Pd parçacıklarına kıyasla Pt'nin eklenmesi parçacık dağılımının homojenliğini arttırmış ve partikül büyüklüğünü azaltmıştır. EDS sonuçlarından ikimetalli nanoparçacıkların heterojen bir karışım olarak bulunduğu gözlemlenmişir. Buna gore Pt açısından zengin olan Pt-Pd parçacıklarının büyüklüğü 3-5 nm arasında iken, Pd açısından zengin olan parçacıkların büyüklüğü 10 nm'yi bulmaktadır.

**Anahtar kelimeler:** süperkritik depozisyon, karbon, nanoparçacıklar, platinyum, paladyum, metal sağlayıcılar.

**ACKNOWLEDGEMENTS**

I would like to thank my research supervisor Professor Can Erkey for his guidance during the progress of this research project. With his help, I also had a chance to experience some important components of academic life by participating and making oral presentations at the international conferences and writing journal papers. I will always remember him with his kindness, friendly attitude towards his students and honesty. I would also like to thank Professor Mehmet Somer for his contributions in understanding the results of the XRD analysis and comments for the questions in my research. I am also grateful to Professor Metin Türkay for supporting me during my graduate studies and to Professor Mark Aindow and the members of his research group at the University of Connecticut for supplying the TEM images and EDS results.

Next, I want to thank to Cevriye Koz and İlkin Kokal for their help in making XRD analysis and to Pınar Çetin for her help in laboratory.

Finally, I want to thank my family for their support.

**TABLE OF CONTENTS**

## NOMENCLATURE

| | |
|---|---|
| $T_C$ | critical temperature |
| $P_C$ | critical pressure |
| $\rho_C$ | critical density |
| $\eta$ | viscosity |
| $q$ | uptake amount of organometallic precursor on substrate |
| $C$ | concentration of organometallic precursor in supercritical phase |
| $K_1$ | Langmuir adsorption constant |
| $Q_0$ | adsorption capacity |
| $K_1Q_0$ | relative affinity of the organometallic precursor towards the surface of the adsorbent |
| $S$ | area covered by organometallic precursor on the substrate surface |
| $A$ | Avogadro's number |
| $r$ | radius of organometallic molecule |
| $(N_A)_e$ | diffusion flux of the organometallic precursor in supercritical phase to the porous volume in the substrate |
| $D_e$ | effective diffusivity for diffusion in porous catalysts |
| $\varepsilon_p$ | porous solid porosity |
| $D$ | diffusivity in case of bulk diffusion in the absence of surface diffusion |
| $\tau$ | tortuosity |
| $F(\lambda)$ | size restriction factor |
| $\lambda$ | ratio of solute diameter to pore size |
| $d_S$ | solute diameter of organometallic precursor |
| $d_P$ | pore size of the substrate particles |
| $S_C$ | Schmidt number at high pressure |
| $Sc^*$ | Schmidt number at atmospheric pressure |
| $Sc^+$ | Schmidt number at high pressure to that at atmospheric pressure |
| $a_i$ | constant in correlation of Schmidt number with solvent molar volume |
| $c_i$ | constant in correlation of Schmidt number with effective hard-sphere packed volume |
| $v_0$ | hard-sphere-closest-packed volume of solvent molecules |
| $v$ | molar volume of solvent |
| $\sigma_1$ | hard sphere diameter of the solute |

| | |
|---|---|
| $\sigma_2$ | hard sphere diameter of the solvent |
| $M_1$ | molecular weight of the solute |
| $M_2$ | molecular weight of the solvent |
| $D_{AB}$ | binary diffusion coefficient |
| $C_{A,s}$ | concentration of $Pd(acac)_2$ in the supercritical phase at the surface of the substrate |
| $C_{A,b}$ | concentration of $Pd(acac)_2$ in the bulk supercritical phase |
| $t$ | time |
| $V$ | volume of $scCO_2$ |
| $m$ | mass of substrate particles |
| $\rho_p$ | density of the porous substrate particles |
| $S$ | external surface area of the substrate particles |
| $C_{A0}$ | initial concentration of $Pd(acac)_2$ in $scCO_2$ at t= 0 |
| $d_{XRD}$ | X-ray diffraction average particle size of the metallic nanoparticles |
| $\lambda_w$ | wavelength of X-ray |
| □ | angle at the peak maximum |
| $\beta_{1/2}$ | width of the peak at half height |

**LIST OF FIGURES**

## LIST OF TABLES

# 1. INTRODUCTION

Metal nanoparticles supported on high surface area carbon substrates are used extensively as catalysts for a wide variety of reactions. Among these catalysts, carbon supported single Pd and bimetallic Pd-Pt catalysts are commonly used for hydrogenation reactions in the fine chemical industry [1]. Furthermore, bimetallic Pd-Pt catalysts show potential for the oxygen reduction reaction (ORR) in electrochemical fuel cells [2], catalytic oxidation of sulfur dioxide in exhaust gas treatment, hydrogen peroxide production and hydrogenation of aromatics [3]. Carbon supported single and binary metal nanoparticles are prepared by a variety of methods including molecular-capping-based colloidal synthesis [4], microemulsion method [5], impregnation [6], sonochemical method [7], modified polyol reduction [8] and deposition-precipitation method [9]. The catalytic properties of such materials depend strongly on the preparation method.

The supercritical fluid deposition technique has recently been receiving increased attention for the preparation of carbon supported catalysts. This process involves the dissolution of an organometallic precursor (OM) in a supercritical fluid and the exposure of the carbon support to the solution. After adsorption of the precursor onto the support, the metallic precursor is converted to its metal form by chemical or thermal reduction. This technique has been used to prepare nanoparticles of a wide variety of metals including Pt, Pd, Ru and Rh supported on various types of carbon substrates [10, 11, 12, 13, 14, 15, 16, 17]. Functionalized multi-walled carbon nanotubes (MWCNTs) were decorated with Pd, Rh and Ru nanoparticles using $Pd(hfa)_2.xH_2O$ (hfa= hexafluoroacetylacetonate), $Rh(acac)_{2.}xH_2O$ (acac= acetylacetonate) and $Ru(acac)_3.xH_2O$ as the organometallic precursors [17]. The reductions were carried out in supercritical carbon dioxide ($scCO_2$)

using hydrogen. Transmission electron microscopy (TEM) results showed well-dispersed Pd nanoparticles with a size range of 5-10 nm, Rh nanoparticles with a size range of 3-5 nm and Ru nanoparticles with very small diameters around 1 nm anchored onto the external walls of MWCNTs. Preliminary cyclic voltammetry (CV) tests indicated that the Pd/MWCNT exhibited a high catalytic activity for hydrogenation of olefins in $CO_2$ as well as a high electrocatalytic activity for the ORR indicative of its potential for fuel cell applications [15]. The supercritical deposition technique was also used to prepare highly dispersed Pt nanoparticles on carbon aerogel (CA) supports using dimethyl (cyclooctadiene) platinum (II) ($PtMe_2COD$) as the precursor [10, 11]. The reduction was carried out at atmospheric pressure under $N_2$ flow at 200 $^0$C and the average size of the Pt particles was as low as 1 nm at a Pt loading of 10 wt%. Zhang et al. [14] prepared CA supported Ru nanoparticles by adsorption of $Ru(acac)_3$ and/or $Ru(cod)(tmhd)_2$ ($cod(tmhd)_2$=bis(2,2,6,6-tetramethyl-3,5-heptanedionato)(1,5cyclooctadiene)) from $scCO_2$ followed by thermal reduction at atmospheric pressure under $N_2$ flow at temperatures between 300-1000 $^0$C. The Ru nanoparticles were dispersed homogeneously throughout the CA support with average particle sizes ranging from 1.7 to 3.8 nm and the mean size of the ruthenium particles increased with increasing reduction temperature. In a study by Bayrakceken et al. [13], various carbon supported Pt electrocatalysts were prepared by supercritical deposition and their electrocatalytic performance was investigated by CV. The electrocatalysts were prepared by adsorption of $Pt(cod)me_2$ onto carbon supports at 70 $^0$C and 24.2 MPa for 6 hours. After depressurization, the impregnated precursor was reduced thermally under flowing $N_2$ for 4 hours at 200 $^0$C. The carbon supports included MWCNTs (internal diameter: 1-3 nm, external diameter: 3-10 nm, length: 0.1-10 μm), Vulcan XC 72R (VXR) and Black Pearl 2000 (BP2000). The X-ray diffraction (XRD) and TEM results showed that the Pt particle sizes were 1.2 nm, 2 nm and 1 nm for Pt/VXR, Pt/MWCNT and Pt/BP2000, respectively. It was found that Pt/VXR catalyst prepared by supercritical deposition showed the best performance for electro-oxidation and hydrogen reduction and its elecrocatalytic activity was substantially higher than that of the commercial Pt/VXR. Although many studies have been conducted to prepare carbon supported single

nanoparticles by $scCO_2$ deposition so far, there is almost no study in the literature regarding the preparation of carbon supported bimetallic nanoparticle utilizing this method.

In this study, carbon black supported single Pd, Pt and bimetallic Pd-Pt nanoparticle catalysts were prepared by $scCO_2$ deposition using $Pd(acac)_2$ and $PtMe_2COD$ as the organometallic precursors. Black Pearl 2000 was used as the carbon support. It has a standard BET surface area of 1450 $m^2/g$, external surface area of 515 $m^2/g$, micropore volume of 0.454 cc/g and a total pore volume of 1.75 cc/g [18]. The preparation of the Pd/BP2000 involved adsorption of $Pd(acac)_2$ from $scCO_2$ solution, followed by chemical reduction in a supercritical mixture of $H_2$ and $CO_2$. The effect of reduction temperature and metal loading on the size of Pd particles was also investigated. The preparation of the Pt/BP2000 involved adsorption of $PtMe_2COD$ from $scCO_2$ solution, followed by chemical reduction in a supercritical mixture of $H_2$ and $CO_2$. In order to prepare bimetallic Pd-Pt/BP2000 catalysts, two different methods were followed. The first is the common method consisting in the deposition of the non-precious metal (Pd) on a previously formed carbon-supported Pt. In the second method, the carbon support was exposed to a solution of $PtMe_2COD$ and $Pd(acac)_2$ dissolved in $scCO_2$ and both of the precursors adsorbed on the surface of the support simultaneously. Subsequently, the precursors were reduced to their metal form by chemical reduction in a supercritical mixture of $H_2$ and $CO_2$. The prepared catalysts were characterized with XRD, TEM and EDS measurements.

The thermodynamics and kinetics of adsorption of the precursors from the $scCO_2$ phase into the carbon phase were also investigated. The thermodynamics of adsorption is described by the equilibrium adsorption isotherm of the OM-$scCO_2$-substrate system at the impregnation conditions which gives the correlation between the concentration of the organometallic precursor in the supercritical phase and the uptake amount of organometallic precursor on the substrate. Knowledge of the adsorption isotherm is necessary to design large scale processes which utilize SCF deposition to prepare supported particles. There is limited data in the literature for adsorption equilibria of organometallic precursors on porous supports. In this study, the adsorption isotherms of $PtMe_2COD$ and $Pd(acac)_2$ on BP2000 in $scCO_2$ were determined at 20 MPa and 60 $^0C$. An adsorption

kinetics model, which was recently developed for describing the kinetics of adsorption of $Ru(cod)(tmhd)_2$ into carbon aerogels from $scCO_2$ solutions [19] was tested for the $Pd(acac)_2$-BP2000-$scCO_2$ system at 20 MPa and 60 $^0$C.

Chapter 2 provides necessary background and literature review on supported Pt-Pd bimetallic nanoparticles and preparation methods, supercritical deposition, solubility of organometallic complexes in $scCO_2$, investigation of the thermodynamics and kinetics of adsorption, preparation of supported single nanoparticles and bimetallic Pt-Pd naoparticles by $scCO_2$ deposition.

Chapter 3 describes the experimental methods which include the adsorption isotherm experiments and the preparation of Pd/BP 2000, Pt/BP 2000 and Pd-Pt/BP 2000 experiments.

The results and discussion of the adsorption isotherms of $Pd(acac)_2$ and $PtMe_2COD$ on BP 2000 and kinetics model development for $Pd(acac)_2$-BP 2000-$scCO_2$ system, XRD, TEM and EDS results of the prepared Pt, Pd and Pt-Pd/BP 2000 catalysts are given in Chapter 4.

The thesis is concluded with a short summary of the performed study and future research work.

# 2 LITERATURE REVIEW

## 2.1 Supported Pt-Pd Bimetallic Nanoparticles and Preparation Methods

Metallic nanoparticles containing more than one species are important materials because they often display properties which are different than those formed from single species. Nanoparticles composed of two different metal elements have drawn a greater interest than monometallic ones in catalysis because it is possible not only to obtain improved catalytic activity but also create new properties [20]. For example; for oxygen reduction reaction in fuel cells, high surface area carbon supported Pt has the highest catalytic activity among the pure metals. However, in order to avoid the kinetic limitations and high costs of Pt, ORR catalysts which are more active and less expensive than Pt resulted in development of alloy catalysts of platinum with various transition metals [21]. The dispersion and the compositional homogeneity of the alloy nanoparticles are important factors to obtain a good elecrtrocatalytic activity. The preparation of supported bimetallic alloys presents some problems with respect to unsupported bulk alloys. The term 'supported alloy' should be distinguished from 'supported bimetallic'. Here, supported bimetallic means two metals present on the same support and not being alloyed [22]. Supported alloys are commonly prepared starting from the formation of supported platinum (Pt/Support) followed by deposition of the second metal on Pt/Support at high temperatures. However, the thermal treatment at temperatures above 700 $^{0}$C under an inert gas or hydrogen gives rise to an undesired metal particle growth by sintering and coalescence of the platinum particles which may result in the decrease in Pt mass activity for the ORR since the mass activity of highly dispersed Pt catalysts decreases for particle

sizes above 5.5 nm. In order to prevent the growing of particles, an alternative method which involves the simultaneous impregnation on the support of Pt and M (M= first row transition metals) precursors, followed by reduction at low (<100 $^0$C) or intermediate temperatures (200-500 $^0$C) is preferred. There are some key parameters in the preparation of carbon supported Pt alloys which are given below:

1. The actual Pt:M (M= first row transition metals) atomic ratio which may be different than expected from the concentrations of the precursors used in the preparation.
2. The amount of M actually alloyed which may be lower than the total M content in the catalyst.
3. The metal particle size since the electrocatalytic activity depends on the metal surface area [21].

Among the supported bimetallic catalysts, Pd-Pt catalysts are commonly used for hydrogenation reactions in the fine chemical industry [1], they show potential for the oxygen reduction reaction (ORR) in electrochemical fuel cells [2], catalytic oxidation of sulfur dioxide in exhaust gas treatment, hydrogen peroxide production and hydrogenation of aromatics [3]. Pd is more abundant and cheaper than Pt and its long-term stability in acidic media may be comparable with Pt but its catalytic activity towards the oxygen reduction reaction (ORR) is lower than that for Pt and its alloys. In the study by Li et al. [23], Pd-rich carbon supported Pd-Pt electrocatalysts were synthesized via a one-step reduction route in order to enhance the activity for methanol tolerant oxygen reduction reaction. The prepared Pd-Pt bimetallic nanoparticles exhibited a single-phase fcc structure. The cyclic voltammetry studies displayed that the electrocatalytic activity of the Pd-Pt/C alloy catalysts was much higher than single metallic Pd/C catalyst. As can be seen from Figure 2.1., the TEM image of the prepared $Pd_3Pt_1$/C and its corresponding particle size distribution histogram shows that $Pd_3Pt_1$ alloy nanoparticles are well dispersed on the

surface of the carbon support with a relatively narrow size distribution and the mean particle size is about 4.8 ±0.7 nm in diameter.

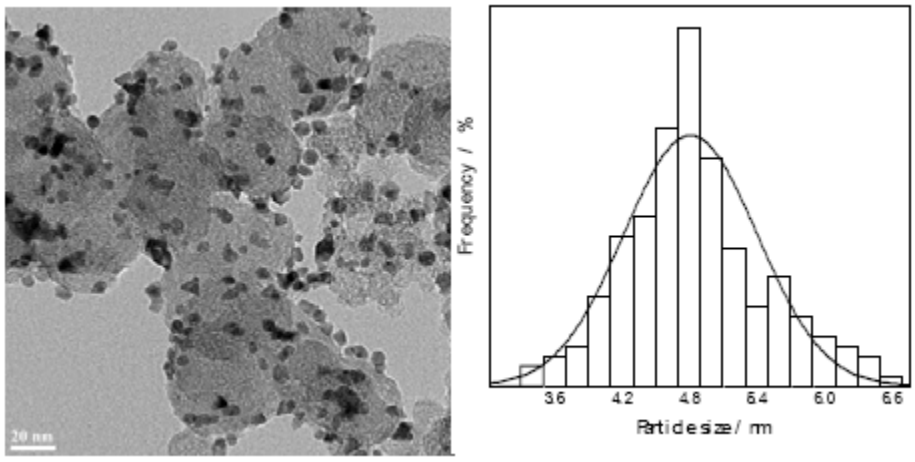


**Figure 2.1:** TEM image of a Pd3Pt1/C catalyst and its corresponding particle size distribution histogram [23].

In the study by Pawelec et al. [24] multi-wall carbon nanotubes (MWNT) supported PtPd particles were prepared and their activity to hydrogenate aromatic rings was compared with other catalyst systems consisting of the same metallic function but changing support substrate ($SiO_2$-$Al_2O_3$ (ASA)) and silica-delaminated zirconium phosphate (ZrPSi)). The PtPd/MWNT catalyst was prepared by simultaneous wet impregnation of the functionalized MWNT support with an aqueous solution of the metal precursors $H_2PtCl_6$ and $H_2PdCl_4$. After adsorption equilibrium had been reached, the excess water was removed until dryness in a rotary evaporator. Catalyst drying was performed in air at 333 K overnight, followed by decomposition of the salts under He at 673 K for 2 h. In order to prepare the ZrPSi supported PtPd nanoparticles, the support was impregnated with an aqueous solution of $PdCl_2$. After adsorption equilibrium had been reached, the excess water was removed in a rotary evaporator. After drying at 383 K in air for 4 h followed by calcination in air at 573 K for 4 h, the Pd/ZrPSi was again impregnated with the required amount of $H_2PtCl_6$ aqueous solution and then dried and calcined under the same conditions.

The PtPd/ASA catalyst was prepared by the adsorption-impregnation method. ASA support was immersed in deionized water into which an aqueous solution of $Pt(NH_3)_4(NO_3)_2$ and $PdCl_2$ of the desired concentration was added. After the adsorption equilibrium had been reached (after contact for 12 h a room temperature), the excess water was removed in a rotary till dryness. Then, the impregnate was dried in air at 383 K overnight and finally calcined in air at 573 K for 4 h at a heating rate of 4 K $min^{-1}$. The platinum and palladium loadings (wt.%) of the catalysts determined by chemical analysis were 0.8 wt.% Pt, 0.7 wt.% Pd for PtPd/MWNT; 1.4 wt.% Pt, 1.7 wt.% Pd for PtPd/ASA and 2.9 wt.% Pt, 1.7 wt.% for PtPd/ZrPSi. The presence of binary Pt-Pd and single Pt and/or Pd phases in the catalysts was monitored by XRD. The reduced PtPd/MWNT sample shows the reflection peaks typical of $Pd^0$ and $Pt_{48}Pd_{52}$ alloy phases derived from the angular shift of the main reflection lines. For this catalyst, the $Pt_{48}Pd_{52}$ and $Pd^0$ XRD particles sizes were quite large; 23.2 nm and 36 nm, respectively. There was no reflection of pure Pt metal phase. For the PtPd/ZrPSi catalyst, a platinum enriched PtPd alloy phase with a molar composition of $Pt_{71}Pd_{29}$ and an XRD size of 16.7 nm was observed. For this catalyst, $Pt^0$ and $Pd^0$ phases were very well dispersed and they were not detected by XRD. On the contrary, there was no alloy phase for the PtPd/ASA catalyst and the XRD size of $Pd^0$ and $Pt^0$ phases were 20 nm and 8 nm, respectively. The XRD patterns of these catalysts are given in Figure 2.2.

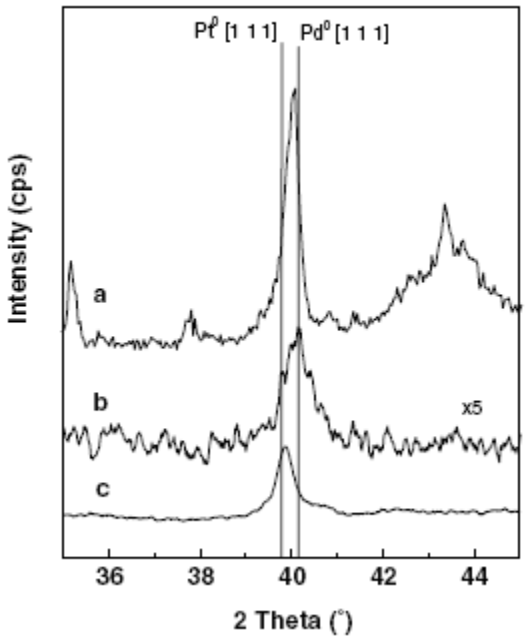


**Figure 2.2:** XRD diffraction patterns of the catalysts (a) PtPd/MWNT (b) PtPd/ASA (c) PtPd/ZrPSi [24].

The estimation of the average metal particle size was done by TEM for these catalysts and they showed the following trend: PtPd/ASA (9 nm) > PtPd/MWNT (7.8 nm) > PtPd/ZrPSi (2.5 nm). As can be seen from the TEM results, there was not consistency between the sizes obtained from XRD and TEM., It can be seen from the TEM images that the largest average particle size belongs to the catalyst where both $Pt^0$ and $Pd^0$ phases exist without alloy phase, then the catalyst with $Pd^0$ phase and PtPd alloy phase rich in Pt follows. According to the TEM images, the smallest size catalyst is the one where there is only PtPd alloy phase rich in Pt content. The TEM image of the PtPd/MWNT is given in Figure 2.3. As can be seen from this figure, most of metallic nanoparticles are located on the external surface of the MWNT.

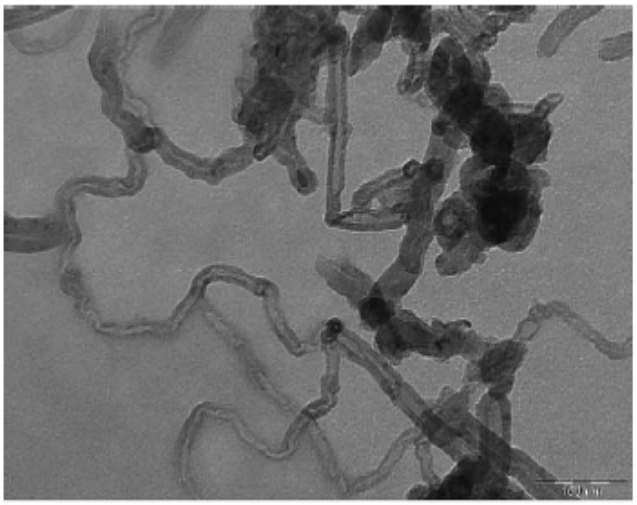

**Figure 2.3**: TEM micrograph of the PtPd/MWNT catalyst [24].

In the study by Li et al. [25] $Pt_3Pd_1/C$, $Pt_1Pd_1/C$ and Pt/C catalysts were prepared in order to provide guidelines for the design of an improved ORR catalyst. Pt-Pd/C catalysts were prepared by a modified polyol process. Predetermined amounts of hexahydrated chloroplatinic acid ($H_2PtCl_6.6H_2O$) and palladium (II) chloride ($PdCl_2$) aqueous solution were added dropwise to carbon suspension under ultrasonic stirring. The pH scaling of the reaction mixture was adjusted to 12-13 using NaOH aqueous solution. The reduction reactions were performed by heating the mixture at 130 $^0$C for 3 h during which purity argon was passed through the reaction system to remove dissolved oxygen. The catalyst was dried in a vacuum oven at 70 $^0$C overnight. The atomic ratios of Pt:Pd was adjusted by changing the amount of the organometallic precursors used. The total metal loading (Pt+Pd) was maintained at 20 wt.% for all the catalysts. The XRD sizes for the prepared catalysts were 2.2 nm for the Pt/C, 2.8 nm for the $Pt_3Pd_1/C$ and 3.6 nm for the $Pt_1Pd_1/C$ catalysts. From the XRD patterns it can be seen that the addition of Pd to Pt/C catalyst has a slight effect on the crystalline structure of the Pt/C because Pt and Pd have almost the same FCC crystalline structure. The corresponding diffraction peak positions of Pt-Pd/C are a little positively shifted with the increment of Pd amount in Pt-Pd/C. The addition of Pd element has a strong effect on the crystalline size of the metal nanoparticles in Pt-Pd/C catalyst. From XRD diffraction data, the particle sizes of Pt/C and $Pt_3Pd_1/C$ are only 2.2 nm

and 2.8 nm, while that of $Pt_1Pd_1/C$ is increased to 3.6 nm. The XRD diffraction patterns of these catalysts are given in Figure 2.4.

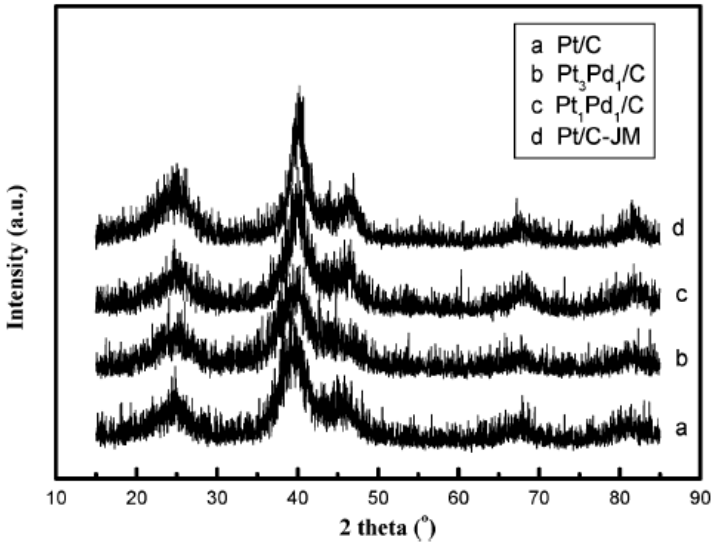


**Figure 2.4 :** XRD patterns of (a) Pt/C (b) $Pt_3Pd_1/C$ (c) $Pt_1Pd_1/C$ (d) Pt/C-JM (commercial) catalyst [25].

TEM results of these catalysts which are given in Figure 2.5 are consistent with the XRD results and show that Pt/C has the smallest nanoparticle size of 2.4 nm, $Pt_3$-$Pd_1/C$ catalyst has a nanoparticle size of 2.9 nm and $Pt_1Pd_1/C$ has the biggest size which is 3.9 nm. All the catalysts in the polyol process are well-dispersed except for the $Pt_1Pd_1/C$ catalyst in which a few agglomerations of metal nanoparticles could be clearly observed which shows that the addition of Pd element in the Pt-Pd/C catalyst not only increases the particle size of the nanoparticles but also changes the dispersion state of the nanoparticles on the carbon support. The distribution of metal nanoclusters in $Pt_1Pd_1/C$ is totally different from that in $Pt_3Pd_1/C$. The HR-TEM image of the $Pt_3Pd_1/C$ catalyst indicates that most of the metal nanoparticles are well-dispersed on the carbon support surface area with bigger area contact between the metal nanoparticles and carbon support, which is similar to the pure Pt/C catalyst. However, for $Pt_1Pd_1/C$ catalyst, a portion of the metal nanoclusters looks like only mixing with the carbon support with less contact area. The different

dispersion morphology of the metal nanoparticles on the carbon support is mainly due to their different nucleus-growth mechanism of metal nanoparticles in $Pt_3Pd_1$/C and $Pt_1Pd_1$/C catalysts. Since Pt takes the majority amount in the $Pt_3Pd_1$/C catalyst, the nucleus-growth mechanism of metal nanoparticles follows the formation model of the Pt/C catalyst [25].

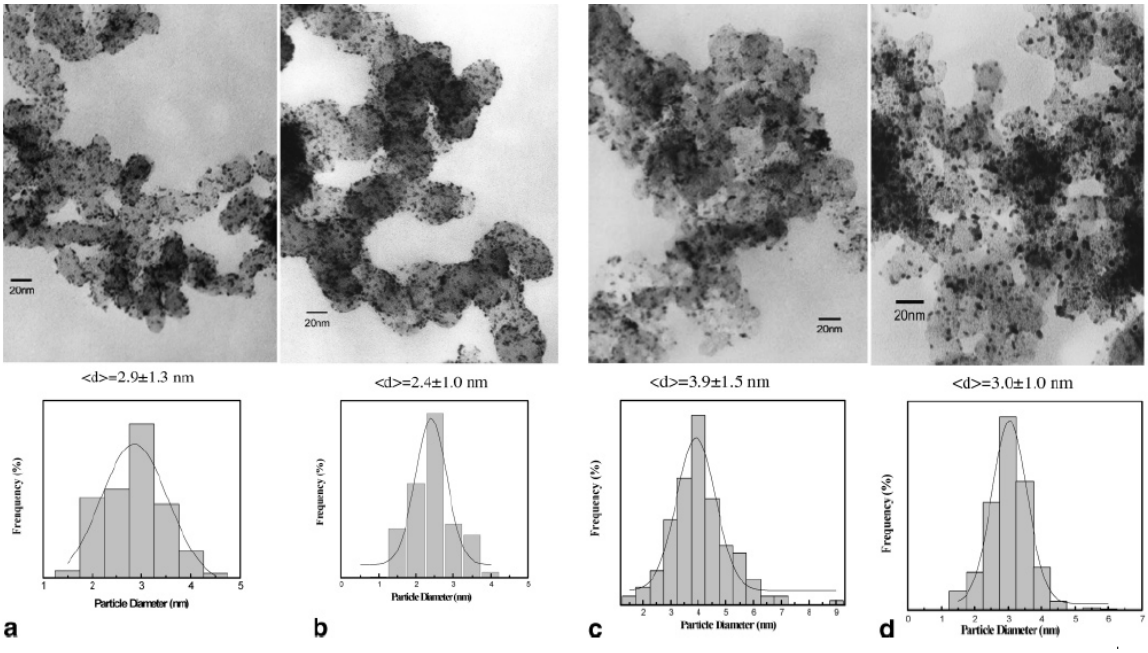


**Figure 2.5:** TEM images and size distributions of the catalysts (a) $Pt_3Pd_1$/C (b) Pt/C (c) $Pt_1Pd_1$/C (d) Pt/C-JM (commercial catalyst) [25].

In order to understand the reactivity of metal alloy surfaces much effort is being invested. In the Pt-Pd system alloy formation and segregation of Pd to the surface of the surface of the bimetallic particles has been observed using EXAFS (extended X-ray absorption fine structure) and TEM (transmission electron miscroscopy) [26]. EXAFS is sensitive to local structure on an atomic scale and constitutes a well-suited experimental technique for the characterization of highly dispersed materials. Based on EXAFS analysis, several studies were conducted to investigate the structure of bimetallic Pt-Pd nanoparticles. One of these studies include structural characterization of colloidal

dispersion of the poly(N-vinyl-2-pyrrolidone)-protected Pd/Pt bimetallic clusters, which were used as the catalysts for the selective partial hydrogenation of 1,3-cyclooctadiene to cyclooctene. The 1.6 nm Pt/Pd (1/1 molar ratio) clusters were described as a modified Pt core structure, in which Pt atoms are connected directly with each other and are located both in the core and on the surface, whereas Pd atoms form islands on the surface. In another study where the influence of mild oxidative environment prepared under air on the structure of alloyed Pt-Pd clusters in contrast to those under nitrogen was made, the segregation of Pd to the surface of bimetallic clusters was concluded from the EXAFS data. In these studies it was reported that there was an alloy formation between Pt-Pd and Pd segregated to the surface of the bimetallic clusters [27]. In the study by Hansen et al. [26], EXAFS investigation of the zeolite supported bimetallic Pt-Pd catalysts was made. With the results obtained, alloy formation and segregation of Pd to the surface of the small bimetallic particles was clearly identified and Pd was found to be enriched at the surface. Some simulations in accordance with the EXAFS results were made. As a result of these simulations, strong surface segregation of Pd in small bimetallic Pt-Pd particles was predicted. Projected snapshot of an equilibrated Pt-Pd cluster is given in Figure 2.6. In this figure the dark circles represent the Pd atoms whereas the white circles represent the Pt atoms [26].

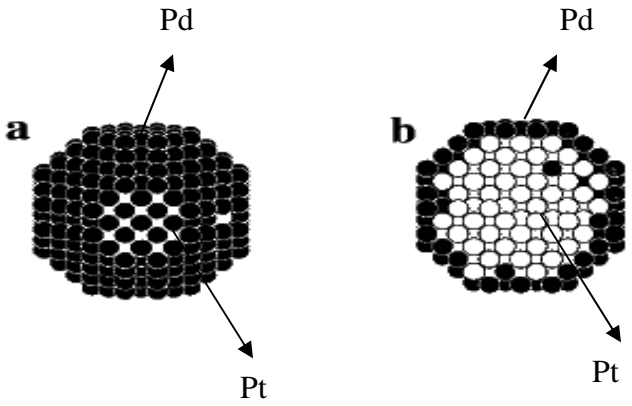


**Figure 2.6** (a) Projected snapshot of an equilibrated Pt-Pd cluster (b) Same snapshot sliced through the center [26].

### 2.1.1 Phase Diagram of the unsupported bulk Pt-Pd alloy

Information about the control of microstructure or phase structure of a particular system is displayed in a phase diagram which is also termed as an equilibrium or constitutional diagram. Phase diagrams are helpful in predicting phase transformations and the resulting microstructures, which may have equilibrium or non-equilibrium character. Phase diagrams represent the relationships between temperature and compositions and the quantities of phases at equilibrium. In Figure 2.7, the phase diagram of the Pt-Pd binary alloy is given. The phase diagram of the Pt-Pd system is similar to that of the Cu-Ni system. The composition ranges from 0 wt.% Pt (100 wt.% Pd) on the left horizontal extremity to 100 wt.% Pt (0 wt.% Pd) on the right. Three different phase regions appear on the diagram; a solid field, a liquid field (L) and a two phase solid+liquid field. Each region is defined by the phase or phases that exist over the range of temperatures and compositions delimited by the phase boundary lines.

The liquid L is a homogeneous liquid solution composed of both Pt and Pd. The solid phase is a substitutional solid solution consisting of both Pt and Pd atoms and having an FCC crystal structure. At temperatures below about 1555 $^{0}$C Pd and Pt are mutually soluble in each other in the solid state for all compositions. The line separating the liquid and liquid+solid phase is termed as the liquidus line. The liquid is present at all temperatures and compositions above this line. The solidus line is located between the solid and the solid+liquid regions below which only the solid phase exists. The solidus and liquidus lines intersect at the two composition extremities which correspond to the melting temperatures of the pure components. In this phase diagram the melting temperatures for the pure Pd and Pt are 1555 $^{0}$C and 1769 $^{0}$C, respectively. Heating pure Pd corresponds to moving vertically up the left-hand temperature axis. Pd remains solid until its melting temperature is reached. The solid-to-liquid transformation takes place at the melting temperature and no further heating is possible until this formation has been completed. For any composition other than pure components, the melting phenomenon will occur over the range of temperatures between the solidus and liquidus lines and both the solid and the liquid phases will be in equilibrium in this temperature range [28]. For the Pd-Pt phase diagram various

measurements of physical properties of Pd-Pt alloys indicate the existence of a continuous solid solution in the Pd-Pt system and the liquidus and solidus lines were sketched based on this information. In the solid phase, the existence of immiscibility with the critical temperature of about 770 $^0$C was predicted based on the difference in the melting points of Pd and Pt [29].

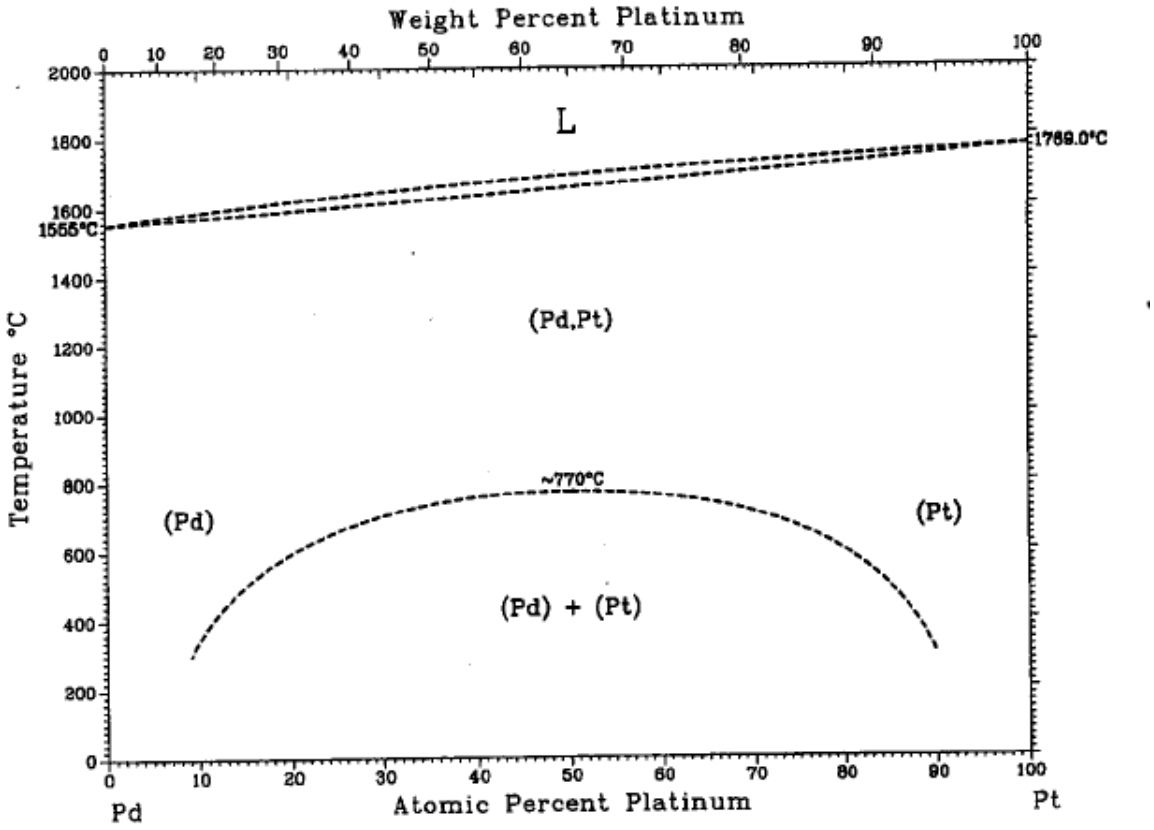


**Figure 2.7:** Pd-Pt phase diagram of the unsupported bulk Pt-Pd alloy [29].

It is well known that nanoscale materials often have different chemical and physical properties than those that characterize similar composition in the bulk. The finite size of nanoscale materials leads to perturbations which result in new nonbulk-like behaviors [30]. For example in the study by Nashner et al. [31], bimetallic Pt-Ru nanoparticles 1.5 nm in diameter were synthesized from molecular precursors with a 1:5 Pt:Ru ratio which assume

a face-centered cubic (fcc) closest-packed structure but bulk alloy of this composition would assume a hexagonal-closest packed (hcp) structure. This simple data point suggests that an interesting divergence may exist between the structural properties predicted by the bulk binary phase diagram and those exhibited by very small supported clusters. Although bulk phase diagrams for many bimetallic materials have been studied extensively, it is unclear whether they can be extended to the nanometer sized regime as a large fraction of atoms reside on the surfaces when size of the particles become small. Surface atoms can contribute significantly to the increment of Gibbs free energy and result in a large difference in property between nanoparticles and bulk materials such as melting point and crystal order. The large fraction of atoms on the surface and at interfaces of bimetallic nanoparticles should affect their phase behaviors. Another important phenomenon in order to obtain the phase behavior is surface segregation of bimetallic nanoparticles in which chemical composition at the surface differs from that in bulk. Surface segregation becomes obvious when the difference in atomic size, surface energy and strain energy given between two elements is large. The surface atoms can reconstruct to form core-shell, sandwich and onion-like structures. The miscibility of individual element in the bimetallic nanoparticles is important in order to understand the structure and property [32]. However; bulk binary phase diagram gives a clue in predicting the alloying temperature and composition of elements in the alloy. Development of binary phase diagrams for the metallic nanoparticles is necessary in order to understand the relationship that exists between composition, size and structure adopted which could provide new insights leading to the useful catalytic activities of metallic nanoparticles [29].

A linear relationship between lattice parameter and composition is described by Vegard's law which can be a good indication of miscible binary alloys that form solid solution. Vegard's law is an approximate empirical rule which holds that a linear relation exists at constant temperature between the crystal lattice constant of an alloy and the concentrations of the constituent elements [32]. This relation can be described by the following following empirical equation 2.1:

$$a = a_2 \times \left( 1 + \frac{a_1 - a_2}{a_2} \times x_1 \right) \quad \textbf{(2.1)}$$

Where; a, $a_1$ and $a_2$ are lattice parameters for the binary solid solution and the two corresponding pure metals, respectively and $x_1$ is the molar fraction of component 1. The lattice parameter is found from the X-ray diffraction characterization. The lattice parameter denoted by 'a' can be determined according to the following relation given in equation 2.2:

$$a = \frac{\lambda}{2\sin\theta} \times \sqrt{h^2 + k^2 + l^2} \quad \textbf{(2.2)}$$

Where; λ is the wavelength of X-ray which equals to 1.5405 Å (for Cu Kα source), Θ is the diffraction angle and h k l are the Miller indices [32]. The relationship between lattice parameter and Pt-Pd binary alloy nanostructure is given in Figure 2.8.

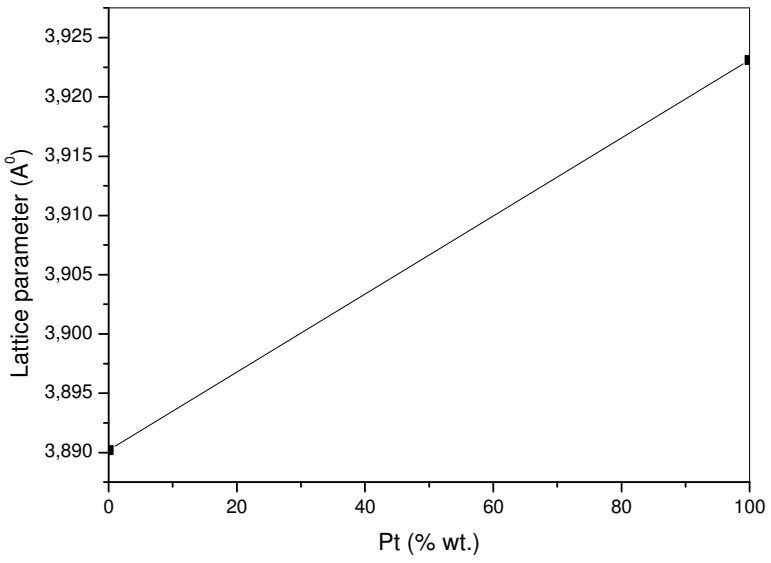


**Figure 2.8:** Relationship between lattice parameter and composition of Pt-Pd binary alloy nanostructures.

## 2.2 Supercritical Deposition

### 2.2.1 Supercritical Fluids

A fluid is said to be supercritical when its temperature and pressure exceed the critical temperature ($T_C$) and pressure ($P_C$). In Figure 2.9, the density and organization of pure fluid molecules in solid, liquid, gas state and supercritical domain are given. At the critical point, the density of the gas and liquid phases becomes equal and the interface between the gas and liquid disappears. The macroscopic behavior of these fluids is characterized by mechanical and thermal instabilities which result from the singular behavior of some properties such as the isothermal compressibility. The microscopic behavior of these fluids can be interpreted by local flactuations of the local density. The local organization includes regions of both gas and liquid local densities. This local organization is dynamic with a life time of approximately 100 ps and a strong function of both temperature and pressure. The local organization provides explanation of the increase of the fluid compressibility. When the case of a high-pressure vessel with a volume V filled with n molecules at temperature T is taken into account, the fluid in this high-pressure vessel can be described as a system consisiting of microdomains with localized densities of both gaseous and liquid levels that are in dynamic equilibrium. When the V (constant T & n) is reduced with a mechanical action, the particles in a microdomain with a local density like a gas will go to a microdomain with a local density like a liquid. This system reaction leads to a very weak increasing of pressure and explains the high value of the fluid compressibility. When, a solute dissolves in a supercritical fluid, the interactions between the solute and the solvent at small distances are taken into account regarding the classical description of solvation but the interactions at long distances are considered by the evaluation of the solute partial molar volume due to the critical behavior of the fluid. The large volume contraction is dependent on the solvent structure and intermolecular forces. When an attractive mixture is taken into account, the addition of a solute causes a change in the solvent organization and generates the aggregation of solvent molecules close to the solute which is dependent on the local flactuations of density [33]. This phenomenon is shown in Figure 2.10: (a) and (b).

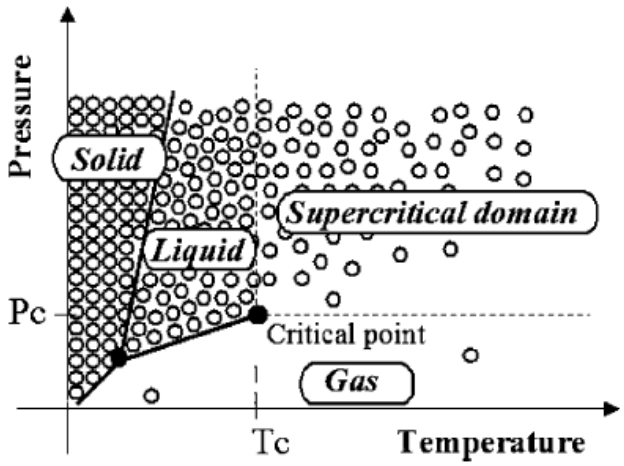


**Figure 2.9:** Schematic representation of microscopic behavior of a pure fluid in the P-T plane phase diagram [33].

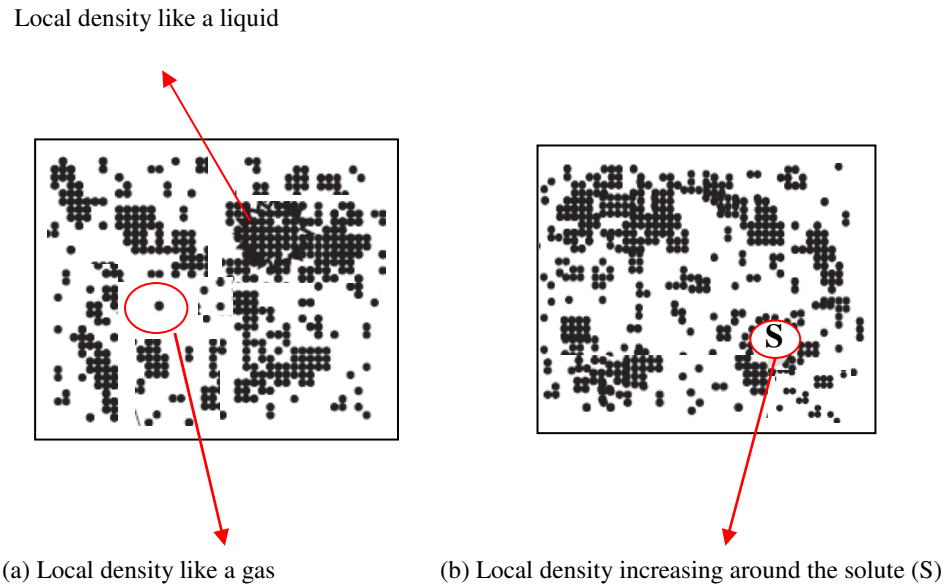


**Figure 2.10:** (a) Schematic respresentation of the molecule distribution in a supercritical fluid (b) solvent and solute molecules in a supercritical solution [33].

Supercritical fluids have unique properties which enable the manipulation of the reaction environment such as viscosity, diffusivity, density and surface tension by changing the temperature and pressure, from gas-like to liquid-like properties [34].The physical properties of these fluids like density, viscosity and diffusivity are intermediate between those of liquids and gases. The thermophysical properties comparison table of fluids is given in Table 2.1.

**Table 2.1:** Characteristic magnitudes of thermophysical properties of fluids [34].

| **Fluid** | **Liquid** | **Supercritical fluid** | **Gas** |
|---|---|---|---|
| Density ($\rho$) ($kg/m^3$) | 1000 | 100-800 | 1 |
| Viscosity ($\eta$) (Pa s) | $10^{-3}$ | $10^{-4}$-$10^{-5}$ | $10^{-5}$ |
| Diffusion coefficient ($m^2/s$) | $10^{-9}$ | $10^{-8}$ | $10^{-5}$ |

Supercritical fluids are widely used in a large area of applications like materials processing, especially for the formation of particles, fibres, thin films (pharmaceuticals, explosives, coatings), drying highly porous gels, petroleum-chemistry separation and purification, food industry, polymer recycling and chromatography. The reason for current industrial and scientific interest in supercritical fluids is that these fluids have the capability of replacing toxic industrial solvents and the ability of tuning solvent characteristics for highly specific separations or reactions [15]. In practice, since the supercritical fluids are close to their $T_C$ and $P_C$, their density is close to $\rho_C$ [35]. In Table 2.2, the comparison of the critical coordinates ($T_C$, $P_C$, $\rho_C$) of some most usual pure fluids are given.

**Table 2.2:** $T_C$, $P_C$ and $\rho_C$ comparison of some most usual pure fluids [35].

| Fluid | $T_C$ ($^0$C) | $P_C$ (MPa) | $\rho_C$ (kg/m$^3$) |
|---|---|---|---|
| Ammonia | 132.4 | 11.29 | 235 |
| Water | 374.1 | 22.1 | 317 |
| Ethane | 32.5 | 4.91 | 212 |
| Ethylene | 9.5 | 5.06 | 220 |
| Propane | 96.8 | 4.26 | 225 |
| n-Pentane | 196.6 | 3.37 | 232 |
| Cyclohexane | 279.9 | 4.03 | 270 |
| Methanol | 240.0 | 7.95 | 275 |
| $CO_2$ | 31.2 | 7.38 | 468 |
| Ethanol | 243.1 | 6.39 | 280 |
| Acetone | 235.0 | 4.76 | 273 |
| Isopropanol | 235.6 | 5.37 | 274 |

Among the supercritical fluids, $scCO_2$ which is readily accessible with a $T_C$ of 31.2 $^0$C and a $P_C$ of 7.38 MPa as shown in Table 2.2, is attractive since it is abundant, inexpensive, non-toxic, non-flammable, environmentally benign and leaves no residue [15]. Besides the environmental benefits, the transport properties of $scO_2$, such as high diffusivity, low viscosity and zero surface tension promote rapid mass transfer within confined geometries and thus can provide conformal step coverage and superior gap-filling ability. The density of $scCO_2$ can approach or exceed those of liquids which enables dissolution of various metal precursors and deposition at relatively high precursor concentrations [36].

In order to understand the solvent characteristics of supercritical fluids, $CO_2$ can be taken as an example. As the critical point of a gas such as $CO_2$ is approached, its isothermal compressibility tends to go to infinity which means that the density of the gas changes rapidly near its critical point. As the density increases, the gas becomes a supercritical solvent and begins to take on the solvent characteristics of a liquid. Therefore, the attraction forces between solvent and solute increase. The solubility of one component in another depends on the intermolecular forces between these components which include attractive forces like induction, dipole-dipole, dipole-induced dipole; repulsive forces like hard sphere type-electron overlap and chemical forces like donor-acceptor complexing and hydrogen bonding. Since all of these forces act over a distance, for example; dispersion and

dipole forces are proportional to $1/r^6$ (r: the distance between molecules), it is reasonable to expect the increase of the solvent power of a supercritical fluid as the system density increases [37].

### 2.2.2 Solubility of metal complexes in $scCO_2$

The fact that solids can dissolve in compressed gases like $scCO_2$ has attracted a great deal of interest. A useful rule of thumb is that $scCO_2$ has solvent properties which is similar to n-hexane except for the fluorinated compounds which have a high solubility in $scCO_2$ but low solubility in alkanes. Generally, the solubility of a compound in $scCO_2$ is related to its vapor pressure. The compounds having higher vapor pressure have higher solubility in $scCO_2$ in the limit of the gas is totally miscible with the fluid. Also, the solubility at a specific temperature increases with increasing pressure thus increasing SCF density but this phenomenon has a limitation. Heating a supercritical solution from its critical temperature under constant pressure leads to a fall in solubility since the density of the fluid decreases but when the temperature is increased further the solubility increases because the vapor pressure of the solute increases faster than the density of fluid drops. This is called retrograde crystallization. When the temperature is increased under constant volume, there is no drop in solubility since the SCF density remains constant [38].

For the production of nanoscale metal particles in $scCO_2$, appropriate metal complexes are required as metal precursors. In order to choose suitable metal complexes, their solubility in $scCO_2$ is important. After experimental investigation of solubility of various ligands in $scCO_2$, it was found that, in general complexes containing cyclopentadienyl and carbonyl ligands exhibit high solubility [39]. The complexes with β-diketonate are also widely used for applications in $scCO_2$. In the study by Lagalante et al. [40], the solubility of copper (II) and chromium (III) β-diketonates in $scCO_2$ was investigated. The results of some experimental mole fraction solubilities in $scCO_2$ at 40 $^0$C and various pressures and thus $scCO_2$ densities found by Lagalante et al. [40] are given in Table 2.3.

**Table 2.3:** Experimental mole fraction solubilities in supercritical $CO_2$ at 40 $^0$C at given pressure and density of some metallic complexes [40].

| **Complex** | **Mole fraction solubility ($\times 10^5$) for given pressure (MPa) (density: g/mL)** | | | | | | | |
|---|---|---|---|---|---|---|---|---|
| | 10.34 (0.652) | 13.79 (0.76) | 17.24 (0.811) | 20.68 (0.847) | 24.13 (0.874) | 27.58 (0.897) | 31.03 (0.916) | 34.47 (0.933) |
| $Cu(tod)_2$ | 26.03 | 49 | 77.51 | 114.1 | 148.8 | 181 | 212.8 | 269.7 |
| $Cu(dmhd)_2$ | - | 3.696 | 15.40 | 20.51 | 26.04 | 32.11 | 34.01 | 36.21 |
| $Cu(dimb)_2$ | 9.170 | 27.26 | 38.6 | 46.19 | 56.13 | 73.05 | 79.42 | 88.41 |
| $Cu(tfbzm)_2$ | - | 0.702 | 1.424 | 2.113 | 2.740 | 3.313 | 3.843 | 4.269 |
| $Cr(acac)_3$ | 1.716 | 6.068 | 9.094 | 11.27 | 13.25 | 15.03 | 17.04 | 19.09 |
| $Cr(thd)_3$ | 400 | 372.2 | 420.8 | 449.4 | 496.6 | 574.0 | 604.9 | - |
| trans-$Cr(tfa)_3$ | 147.9 | 169.1 | 177.3 | 197.4 | 222.4 | 250.6 | 263.8 | 272.1 |
| Cis-$Cr(tfa)_3$ | 67.3 | 87.81 | 113.9 | 135.6 | 142.2 | 160.1 | 170.7 | 190.8 |

$Cu(tod)_2$: bis (pentane-2,4-dionato)copper (II)

$Cu(dmhd)_2$: bis (1,1-dimethylhexane-3,5-dionato)copper (II)

$Cu(dimb)_2$: bis (2,6-dimethylheptane-3,5-dionato)copper (II)

$Cu(tfbzm)_2$: bis (1,1,1-trifluoro-4-phenylbutane-2,4-dionato)copper (II)

$Cr(acac)_3$: tris(pentane-2,4-dionato)chromium (III)

$Cr(thd)_3$: tris(2,2,6,6-tetramethylheptane-3,5-dionato)chromium (III)

Trans-$Cr(tfa)_3$: trans-tris(1,1,1-trifluoropentane-2,4-dionato)chromium (III)

Cis-$Cr(tfa)_3$: cis-tris (1,1,1-trifluoropentane-2,4-dionato)chromium (III)

As can be seen from Table 2.3, Lagalante et al. [40] found that substituting trifluoromethyl for methyl groups as substituent increases solubility, whereas substituting phenyl groups decreases the solubility in $scCO_2$. Experimentally increasing fluorine substitution on the ligands bound to metals increases the solubility of chelates in supercritical $CO_2$. In the study by Yazdi et al. [41], it was proposed that the solubility enhancement after the substitution of fluorine resulted from special interactions of electron rich fluorines in C-F bonds with relatively electron poor $CO_2$ molecules. When the solubilities of cis and trans isomers of the $Cr(tfa)_3$ in $scCO_2$ was compared, it was found that cis-$Cr(tfa)_3$ of which the $CF_3$ groups reside on the same side making it more polar than the trans-$Cr(tfa)_3$ had lower solubility since $CO_2$ molecule has nonpolar nature. From Table 2.3, the solubility of the β-diketonate ligands is expected to be in the order acac < dmhd < dibm < tod < thd for the Cu and Cr- β-diketonates. In some other solubility studies in $scCO_2$, it was found that alkyl groups and long-chain alkyls in the ligands leaded to higher solubility of the complex whereas, aryl groups generally showed lower solubility [39]. In the study by Aschenbrenner et al. [39] , the effect of both of ligands and metal atoms on solubility of metal complexes in $scCO_2$ was investigated. The solubility of various β-diketonate, cyclopentadienyl and cyclooctadiene complexes with metals like silver, copper, nickel, palladium, ruthenium, cobalt, chromium, iron and platinum were examined in $scCO_2$ at 333 K and pressures up to 30 MPa. The solubility data of some of the examined compounds are given in Table 2.4.

**Table 2.4:** Experimental data for the solubility (S) of the investigated metal complexes in carbon dioxide at 60 $^0$C at different pressures and densities [39].

| **Complex** | **S ($\times 10^5$ mol/mol) at given P (MPa) and (ρ (kg/m$^3$))** | | | | | | | | |
|---|---|---|---|---|---|---|---|---|---|
| | 10 (290) | 12 (434) | 12.5 (472) | 15 (604) | 17 (665) | 17.5 (676) | 20 (724) | 25 (787) | 30 (830) |
| $Cu(acac)_2$ | 0 | - | - | 1 | - | - | 2 | - | 3 |
| $Cu(thd)_2$ | 1 | 11 | - | 55 | - | 82 | - | - | - |
| $Ni(acac)_2$ | 0 | - | - | 0 | - | - | 0 | - | 6 |
| $Ni(thd)_2$ | 0 | - | 4 | 12 | - | 18 | 23 | 28 | - |
| $Pd(acac)_2$ | 0 | - | - | 2 | - | - | 4 | - | 6 |
| $Pt(cod)me_2$ | 3 | 20 | - | 65 | 89 | - | 132 | - | - |
| $Ru(thd)_2cod$ | 1 | 7 | - | 56 | - | - | - | - | - |
| $Ru(thd)_3$ | 1 | 16 | - | 174 | - | - | - | - | - |
| $Co(thd)_3$ | 2 | 17 | - | 122 | 213 | - | - | - | - |

$Cu(acac)_2$: Copper(II) acetylacetonate

$Cu(thd)_2$: Bis(2,2,6,6-tetramethyl-3,5-heptanedionato)copper(II)

$Ni(acac)_2$: Nickel(II) acetylacetonate

$Ni(thd)_2$: Bis(2,2,6,6-tetramethyl-3,5-heptanedionato)nickel(II)

$Pd(acac)_2$: Palladium(II) acetylacetonate

$Ru(thd)_2$cod:Bis(2,2,6,6-tetramethyl-3,5-heptanedionato)(1,5-cyclooctadiene)ruthenium(II)

$Ru(thd)_3$: Tris(2,2,6,6-tetramethyl-3,5-heptanedionato)ruthenium(III)

$Co(thd)_3$: Tris(2,2,6,6-tetramethyl-3,5-heptanedionato)cobalt(III)

As can be seen in Table 2.4, at the given experimental conditions, most of the investigated cod and thd complexes exhibited high solubility in $scCO_2$ whereas the acac complexes generally showed quite low solubility. 'thd' complexes almost showed a solubility about one order of magnitude higher than acac complexes. This was explained due to the additional alkyl groups in the thd ligand compared to acac which caused an increase in solubility. This was due to a better shielding of the metal centre atom by the thd ligand. The effect of central metal atom on solubility was also investigated. For this purpose, cyclopentadienyls of iron, ruthenium and osmium which belong to the same group of the periodic table and differ only in atomic mass and size (increasing in the order of Fe<Ru<Os) were used at 333 K. Although the molecular structures and the valance electron configurations were identical, the mass and size of the corresponding cp complexes also increased proportional to the mass and size of the central metal atoms used. Since the normal melting temperature of the investigated complexes increase with molecular mass in the order of $Fe(cp)_2$<$Ru(cp)_2$<$Os(cp)_2$, the intermolecular cohesion also increases. Also, when the distance between the ligands and central atom increases, the shielding of the central atom by the ligands decreases. So, increased intermolecular cohesion and decreased shielding of the central atom decreases the solubility. Therefore, it was found that the solubility of organometallic complexes in $scCO_2$ was higher when the atomic number of the central metal atom decreased [39]. The solubility vs. SCF pressure figure of these complexes are given in Figure 2.11.

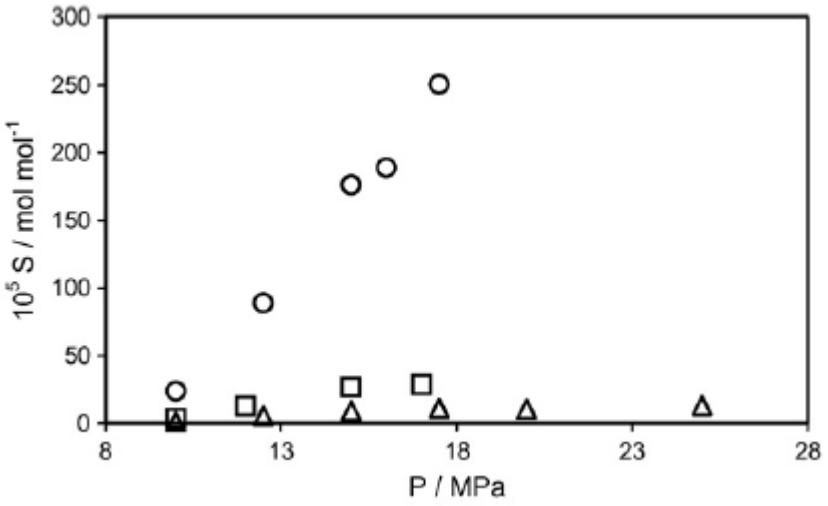


**Figure 2.11:** Solubility (S) of cp complexes of Fe(O), Ru(□) and Os (Δ) in supercritical carbon dioxide at $60^0$C [39].

The organometallic precursors used in this thesis are Pt(cod)$me_2$ and Pd(acac)$_2$. The solubility data given in Table 2.4 for the experiment conditions which are 20 MPa, 60 $^0$C and 724 kg/m$^3$ scCO$_2$ density, is $4\times10^{-5}\,mol/mol\,scCO_2$ and $132\times10^{-5}\,mol/mol\,scCO_2$ for Pd(acac)$_2$ and PtMe$_2$COD [39], respectively. The molecular structures of these organometallic precursors are given in Figure 2.11.

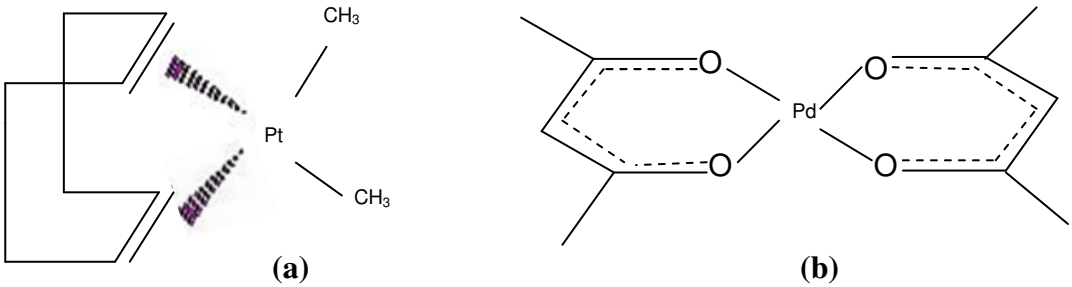


**Figure 2.12:** The molecular structure of (a) PtMe$_2$COD, (b) Pd(acac)$_2$.

### 2.2.3 Investigation of Thermodynamics and Kinetics of Adsorption of Organometallic Precursors on the Substrate from $scCO_2$ Solution

There are no studies on the fundamental aspects of the incorporation of the organometallic precursors on the substrate such as thermodynamics and kinetics of adsorption although it is quite important to understand the dynamics of the adsorption process. It is necessary to measure and study the adsorption isotherms of organometallic precursors on the substrate since the thermodynamic equilibrium between the solid and the fluid phases plays a crucial role in understanding the dynamics of the supercritical fluid deposition process. Equilibrium adsorption data provides information about the interactions between adsorbate-adsorbent and adsorbate-fluid which is necessary for optimizing the adsorption. The thermodynamics of adsorption is described by the equilibrium adsorption isotherm of the OM-$scCO_2$-substrate system at the impregnation conditions and gives the correlation between the concentration of the organometallic precursor in the supercritical phase and the uptake amount of organometallic precursor on the substrate. In this thesis, the adsorption isotherms of $PtMe_2COD$ and $Pd(acac)_2$ on BP2000 in $scCO_2$ were determined and compared at the given experimental conditions. Kinetics model development is important in order to understand the controlling mass transfer resistances and system processing parameters. In this thesis the adsorption kinetics of the $Pd(acac)_2$-BP2000-$scCO_2$ system was investigated by developing a kinetics model taking into account the pore diffusion and local equilibrium in the pores of BP 2000. With the help of this kinetics model, the effect of system parameters like tortuosity, substrate particle size and isotherm parameters on the kinetics of adsorption was investigated.

### 2.2.4 Preparation of Supported Single Nanoparticles by $scCO_2$ Deposition

Many studies have so far been conducted in order to prepare supported nanoparticles with various preparation methods such as sol process, micelles, sol-gel process, chemical precipitation, pyrolysis and chemical vapor deposition [42]. These methods have some drawbacks in controlling over either particle dimensions, including the particle size and distribution or metal concentration in the composites. For example, in chemical

precipitation method, usage of liquid solutions as the processing medium could cause agglomeration of particles and collapse of fragile supports such as aerogels due to the high surface tension of liquid solutions; in sol-gel and micelle process the metallic precursors could interfere with polymerization chemistry in solution; in chemical vapor deposition, the process is often limited by the vapor pressure of the precursor and the processing temperature causing limited mass transfer kinetics [15].

In order to prepare high surface area supported single nanoparticle catalysts, supercritical $CO_2$ incorporation can be used as an alternative and promising way since $scCO_2$ has the capability to replace toxic solvents and the tuning solvent characteristics by adjusting properties from gas to liquid with small pressure and temperature variations and it has high diffusion rates, zero surface tension and low viscosity. This process mainly involves the dissolution of precursors in a dense fluid and exposure of the substrate to the solution. After the incorporation of the support with the precursors, decomposition of the precursors can be accomplished by either chemical reduction in the supercritical fluid (SCF) with hydrogen or thermal reduction in SCF, or thermal reduction in an inert atmosphere or chemical conversion with hydrogen or air after depressurization. The scheme of the process is given in Figure 2.13.

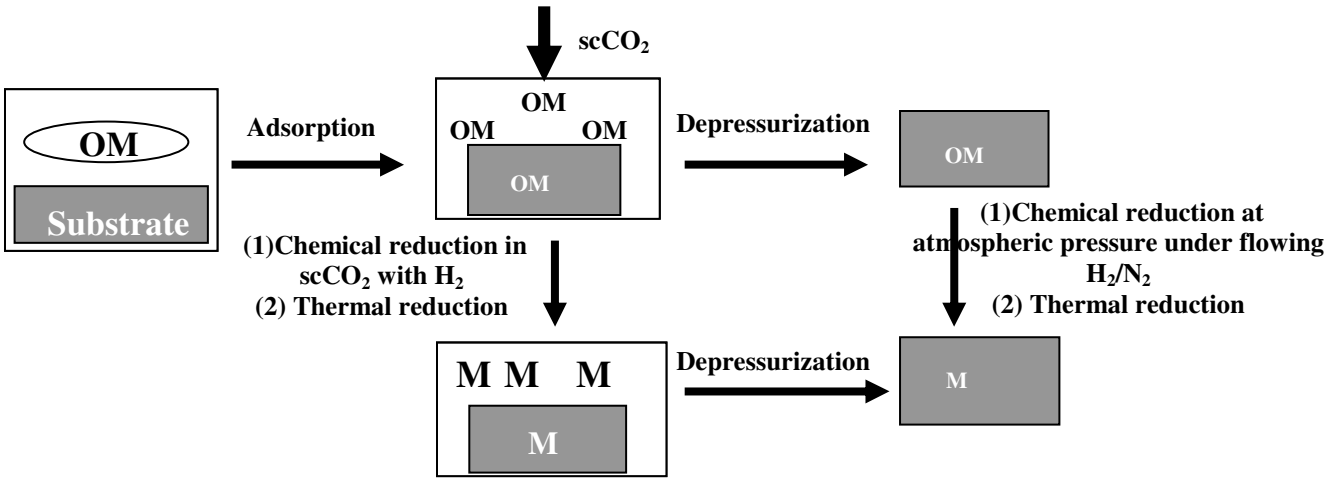


**Figure 2.13:** The scheme of SCF deposition process for the preparation of supported single nanoparticles.

Using SCF deposition process, many studies have so far been conducted in order to prepare supported single nanoparticles like Pt, Pd, Ru, Rh, Ag and Au from their organometallic precursors in $scCO_2$ [12, 13, 14, 15, 16]. In the study by Bayrakceken et al. [13], different types of carbon supported Pt catalysts were prepared and investigated in proton exchange membrane fuel cell applications. $PtMe_2COD$ was impregnated into carbon supports like multi-walled carbon nanotubes (MWCNTs) (internal diameter: 1-3 nm, external diameter: 3-10 nm, length: 0.1-10 μm), Vulcan XC 72R (VXR) and black pearl 2000 (BP 2000) assisted by $scCO_2$ at 70 $^0$C and 24.2 MPa for 6 hours. Subsequent to depressurization, the impregnated precursor was reduced thermally under flowing $N_2$ at 100 $cm^3$/min for 4 hours at 200 $^0$C. The metal loading of the prepared catalysts was found from the weight change by using an analytical balance. The metal content of the samples was determined from the amount of adsorbed precursor assuming that all of the platinum in the adsorbed precursor was reduced to elemental Pt without volatilization during thermal reduction and all the precursor ligands volatilized from the surface of the composites. The XRD results of the synthesized Pt/MWCNT (9.9 wt.%), Pt/BP2000 (47.5 wt.%) and Pt/VXR ( 9 wt.%) and commercially available Pt/C (ETEK-10 wt.%) are given in Figure 2.14.

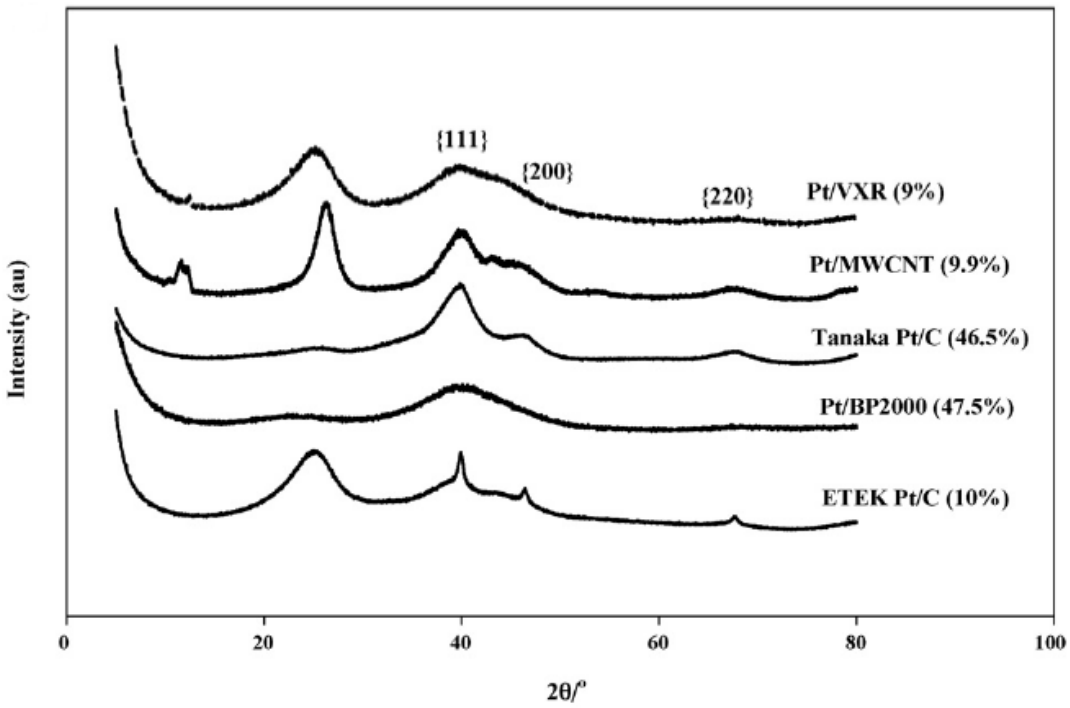


**Figure 2.14:** XRD patterns for the synthesized Pt/MWCNT, Pt/BP 2000, Pt/VXR and commercial ETEK Pt/C catalysts [13].

The Pt particle sizes calculated from Scherrer equation using the half full width at the half maximum of the (2 2 0) reflection were 6 nm, 1.2 nm, 2 nm and 1 nm for the commercial Pt/C (ETEK), Pt/VXR, Pt/MWCNT and Pt/BP2000, respectively. The TEM results for these catalysts are given in Figure 2.15.

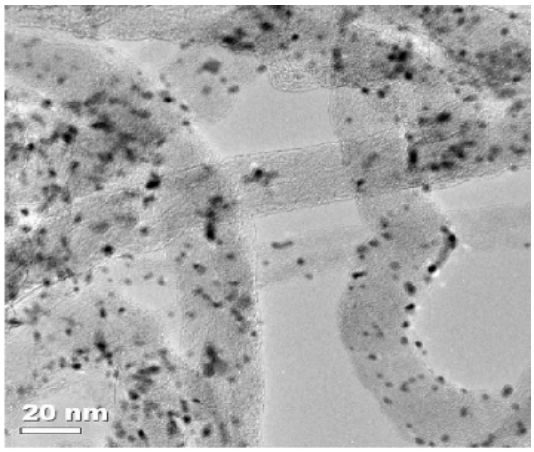


**(a)** Pt/MWCNT

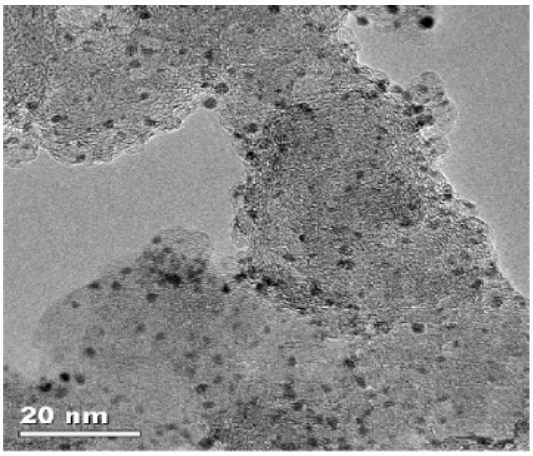


**(b)** Pt/VXR

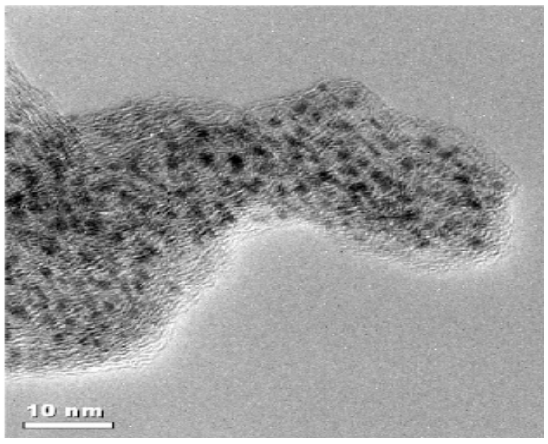


**(c)** Pt/BP 2000

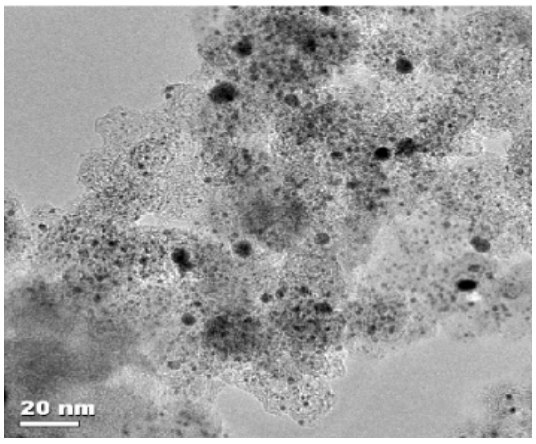


**(d)** Pt/C (ETEK)

**Figure 2.15:** TEM images for different type carbon supported Pt catalysts [13].

There was a good agreement between the average sizes obtained from XRD and TEM data. The average particle sizes of the prepared catalysts were around 1-2 nm with a narrow and homogeneous distribution on the carbon support. Among the carbon supports, the BP 2000 with the highest surface area had the highest Pt loading (47.5 wt.%) in the work done by Bayrakceken et al. [13].

In the study by Howdle's group [43], the preparation of gold nanoparticles into both silica gels and conventional polymers using organic gold compounds via supercritical impregnation followed by hydrogen reduction of the precursors was demonstrated. These catalysts are widely used as low temperature oxidation catalysts. The precursors used were dimethylacetylacetonato gold (III) (Au(acac)$Me_2$) and dimethylhexafluoroacetylacetonato gold (III) (Au(hfac)$Me_2$). Silica, polyamide, polypropylene and polytetrafluoroethylene (PTFE) were used as the substrates. The substrates were impregnated by the precursors in $scCO_2$ at 27.58 MPa and 40 $^0$C for 24 hours. In order to allow for full decomposition and reduction of the infused complex to metal atoms and dissociated ligands, the precursor impregnated substrates were reduced with $H_2$ at 10.34 MPa and 80 $^0$C in batch mode for 24 hours and then depressurized. For the extraction of the dissociated ligands, the system was purged with $CO_2$ for a further 24 hours at 27.58 MPa and 40 $^0$C. The XRD pattern of the prepared Au/Si catalysts is given in Figure 2.16. This pattern belonged to the catalysts processed by Au(acac)$Me_2$ precursor. Unfortunately, Au(hfac)$Me_2$ did not deposit on silica as well as Au(acac)$Me_2$. Howdle's group postulated that the fluorinated ligands in Au(hfac)$Me_2$ preferentially aided the partition of the precursor into the mobile $scCO_2$ phase resulting in poor deposition. As shown in Figure 2.16, XRD patterns obtained for the Au(acac)$Me_2$ processed Au/Si (3 wt.% Au) exhibited a broad reflection corresponding to the amorphous silica matrix and the remaining four reflections were representative of elemental gold showing the fcc structure. The average particle size obtained from Scherrer equation was 6.1 nm.

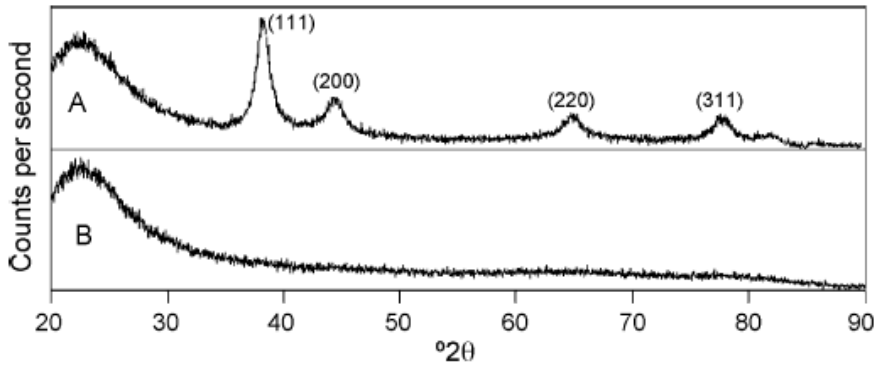


**Figure 2.16:** (a) XRD pattern of silica supported gold nanoparticles (b) XRD pattern for blank silica [43].

As can be seen from the TEM image given in Figure 2.17, gold nanoparticles were homogeneously dispersed throughout the silica samples with average particle size less than 10 nm.

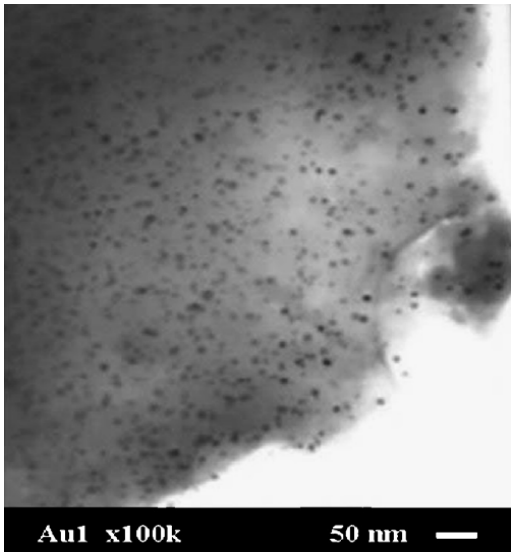


**Figure 2.17:** TEM image of gold nanoparticles deposited on silica processed using the $Au(acac)Me_2$ as precursor [43].

Using the identical conditions, gold nanoparticles were also incorporated into three types of polymers; PTFE, polyamide and polypropylene also. The TEM images of these catalysts are given in Figure 2.18.

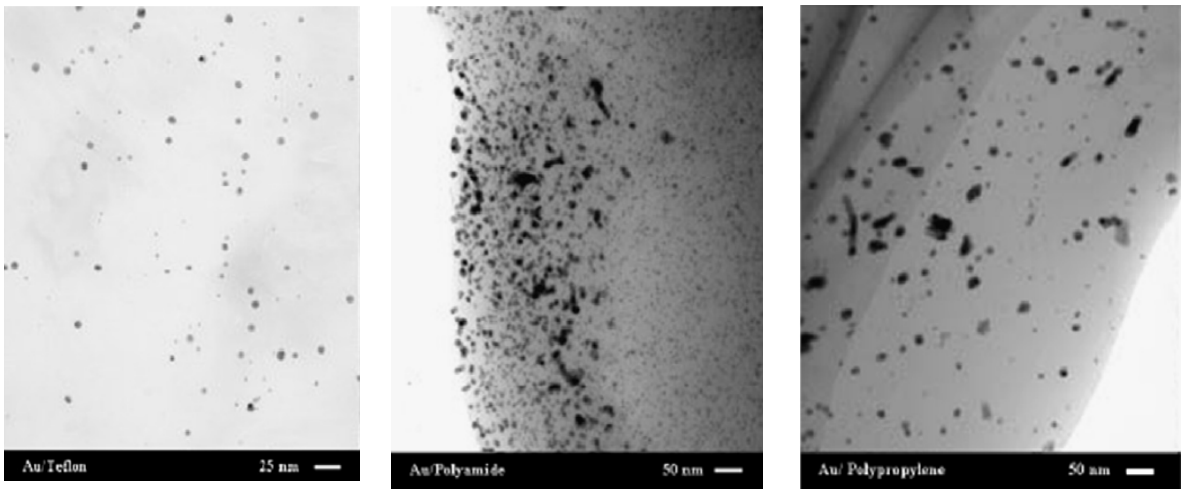


**Figure 2.18:** TEM images of the gold nanoparticles impregnated into (a) PTFE, (b) Polyimide, (c) Polypropylene [43].

As can be seen in Figure 2.18, the particle sizes and shapes of Au were different on each sample and much less homogeneous compared to silica. For the composites where, PTFE was used as the substrate, the average particle size of the Au nanoparticles was found to be 4.4 nm. When polyimide was used as the substrate, there was an inhomogeneous dispersion with small (average particle size: 3.2 nm) and big (average particle size: 18.7 nm) Au nanoparticles differing on the surface and towards the center of the polymer samples, respectively. On polypropylene substrate, there were large erractic, non-circular Au nanoparticles with an average size of 23.1 nm. Howdle's group discussed that the variety of sizes and shapes of nanoparticles in polymers could be affected by interaction between polymers and precursors/nanoparticles and by diffusion of $scCO_2$/precursors inside of the polymers. Polyamide and polypropylene could have lower affinity to $scCO_2$

than PTFE and hence the precursor content in polymer, the rate of depressurizing, the gold particles nucleation and the growth of the particles could all appear significantly different from those obtained in PTFE and inorganic substances [43]. As can be seen from Howdle's group's studies, the effect of support on the properties of the supported nanoparticles is quite important.

Using $scCO_2$ deposition, Ye et al. [17] decorated functionalized MWCNTs with Pd, Rh and Ru, by a simple hydrogen reduction of metal-β-diketonate precursors. The Pd-MWCNT catalysts are widely used in selective hydrogenation of olefins in $CO_2$ and electrochemical reduction of $O_2$. $Pd(hfa)_2.xH_2O$, $Rh(acac)_2.xH_2O$ and $Ru(acac)_3.xH_2O$ were used as precursors. The precursors and MWCNTs were placed in a stainless steel batch reactor and filled with $H_2$-$CO_2$ mixture at 8.1 MPa and kept at these conditions for 30 min. for complete dissolution. For reduction, different temperatures; 80, 250 $^0$C and 250 $^0$C were adopted for Pd, Rh and Ru precursors, respectively and kept at these conditions for 5-10 min. The TEM image of the Pd/MWCNT (10 wt.% Pd) is shown in Figure 2.19 : (a). Well-dispersed, spherical particles were anchored onto the external walls of MWCNTs and the size range of these particles were 5-10 nm. When a commercial 10 wt.% Pd loaded Pd/Activated carbon catalyst was examined by TEM for comparison, Ye et al. [17] found that the results showed numerous very large Pd nanoparticles irregularly distributed on the carbon surfaces. MWCNT was a better support candidate than activated carbon for the preparation of supported Pd nanoparticles with the capability of stabilizing nanometer-sized metal particles on the external surfaces. The TEM image for Rh/MWCNT is given in Figure 2.19: (b). A high and homogeneous dispersion of nanoparticles with a uniform distribution of sizes centered around 3-5 nm was observed. Ru/MWCNT image shown in Figure 2.19: (c). also reveals that Ru nanoparticles dipersed highly with uniform size distribution and very small diameters around 1 nm throughout the full length of MWCNTs.

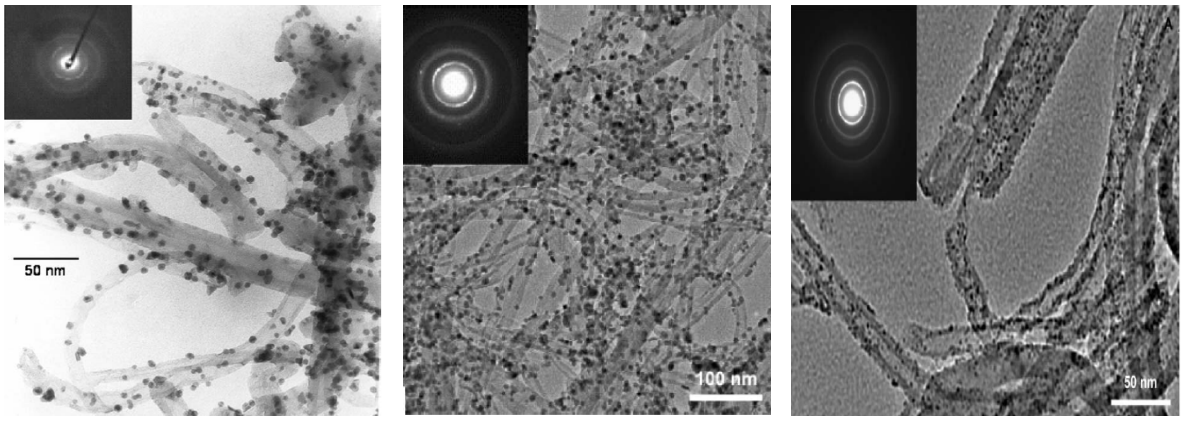


(a) (b) (c)

**Figure 2.19:** TEM images of the MWCNTs decorated with (a) Pd, (b) Rh, (c) Ru [17].

Recently, the synthesis of functional metallic nanoparticles by using the arrested precipitation in $scCO_2$ has also attracted a great deal of interest. Moisan et al. [44] synthesized organic-inorganic hybrid nanoparticles in $scCO_2$ to form stabilized nanoparticles in the organic part consisting of amphiphilically modified dendritic polyamines. A hyperbranched polyethylenimine amide substituted with fluoroalkyl moieties at the chain ends (PEI-CO-$C_{10}H_4F_{17}$) and $Pd(acac)_2$ were placed in a stainless steel batch reactor under $scCO_2/H_2$ ($P_{H2}$= 0.4 MPa, $P_{TOTAL}$= 15 MPa) at 100 $^0$C. The polymer and $Pd(acac)_2$ were insoluble at the given experimental conditions. After depressurization of the reactor, the obtained dry powder hybrid nanoparticles were characterized by TEM as given in Figure 2.20. The results showed that the Pd nanoparticles arrested in the polymer were very well dispersed with an average size of 3.3 nm. As shown in Figure 2.21, when the experiment at the same conditions was carried out without the arresting polymer, the nanoparticles aggregated which proves the effectiveness of arresting polymer stabilization for palladium nanoparticles formation.

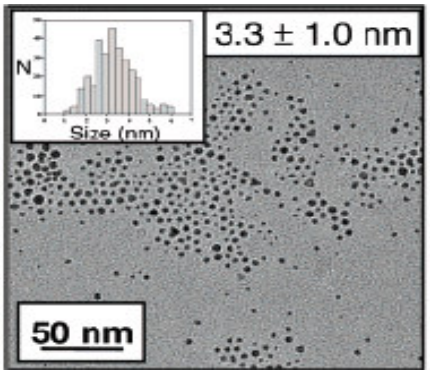


**Figure 2.20:** TEM image of the Pd/polymer hybrid prepared in $scCO_2/H_2$ ($P_{H2}$= 0.4 MPa, $P_{TOTAL}$= 15 MPa) [44].

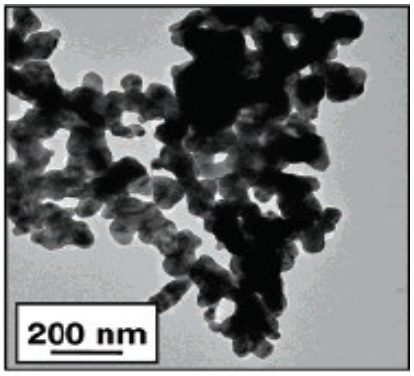


**Figure 2.21 :** TEM image of the Pd aggregates prepared in $scCO_2/H_2$ without the polymer ($P_{H2}$= 0.4 MPa, $P_{TOTAL}$= 15 MPa) [44]**.**

### 2.2.5 Preparation of Supported Bimetallic Pt-Pd Nanoparticles by $scCO_2$ Deposition

Very few studies have so far been conducted for the preparation of supported Pt-Pd bimetallic nanoparticles in $scCO_2$. One of those studies was carried out by Puniredd et al. [20]. In that study, dendrimers with their perfectly branched architecture, monodisperse nature and 3D structure having interior void spaces were used as hosts for the formation of bimetallic Pt-Pd nanoparticles in $scCO_2$. These catalysts were found to be effective in the

partial hydrogenation of 1,3-cyclooctadiene when compared to the monometallic nanoparticles. $Pd(acac)_2$ and $Pt(acac)_2$ were used as the organometallic precursors. Firstly, thin film systems were formed by alternate covalent molecular assembly of pyromellitic dianhydride (PMDA) and second generation polyamidoamine dendrimer (PAMAM) in $scCO_2$ at 40 $^0$C and 10 MPa. Subsequent to depressurization, $Pd(acac)_2$ and $Pt(acac)_2$ were injected inside the dendrimer containing vessel under $scCO_2$ at 10 MPa and 40 $^0$C. The precursor-laden films were reduced thermally and in $scCO_2$. Thermal reduction was carried out by heating the precursor laden dendrimer film samples in presence of air at 300 $^0$C for 12 hours to decompose the acetylacetonate complexes. $ScCO_2$ reduction was carried out by dimethylamine borane in ethanol solution as reducing agent in $scCO_2$ at 10 MPa and 40 $^0$C for 2 hours. The TEM images for the multilayer dendrimer film immobilized Pd-Pt nanoparticles is given in Figure 2.22. From the figure it can be seen that the average sizes of the Pt-Pd nanoparticles were found to be $8 \pm 2$ nm and $1.25 \pm 0.25$ nm, for thermal and $scCO_2$ reduction methods, respectively. During thermal reduction, the loss of the dendrimer resulted in aggregation of particles, whereas the continued presence of the dendrimer structure restricted the aggregation, stabilizing the nanoparticles and resulting in smaller sizes. From the energy dispersive X-ray analysis (EDS), the average composition for Pt-Pd nanoparticles (Pd:Pt= 1:1 molar ratio) was 60 wt.% Pd and 40 wt.% Pt.

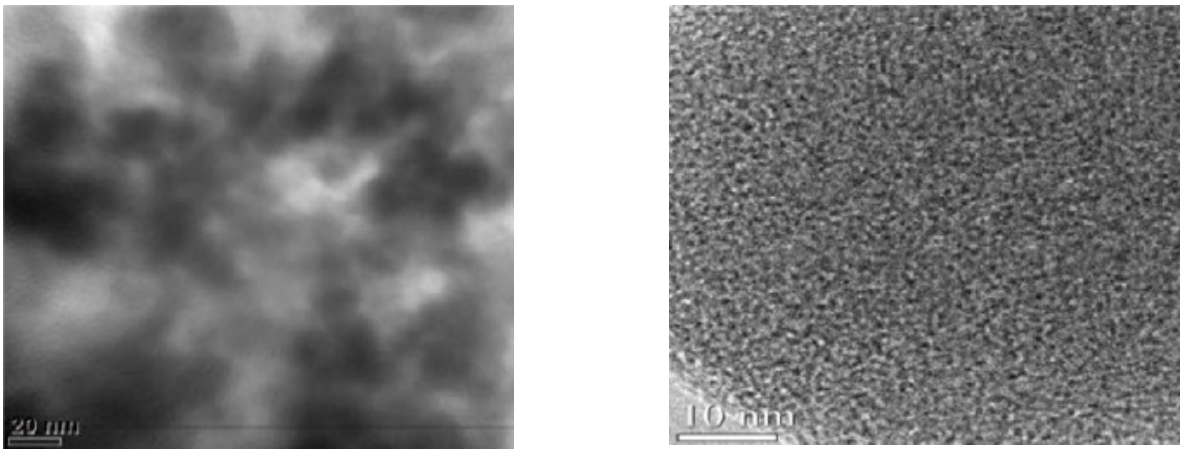


**(a)** **(b)**

**Figure 2.22:** TEM results for Pd-Pt nanoparticles (Pd:Pt= 1:1 (molar ratio)) from (a) Thermal reduction (b) $ScCO_2$ reduction [20].

In another study by Yen et al. [45], Pt-Pd bimetallic nanoparticles were deposited on multiwalled carbon nanotubes (MWCNTs) in $scCO_2$ using platinum acetylacetonate ($Pt(acac)_2$) and palladium hexafluoroacetylacetonate ($Pd(hfac)_2$) as the organometallic precursors. The precursors and the MWCNTs were placed in a high pressure reaction cell of 10 mL volume and 100 atm of $CO_2$ was added into the cell in order to dissolve the metal precursors for 1 h. For both dissolution and reduction of the bimetals 200 $^0$C was selected. After 1 h, a mixture of $H_2$ at 10 atm and $CO_2$ at 240 atm was injected into the cell which combined to a final pressure of 250 atm. After 30 min. of reduction, the cell was depressurized and cooled down to room temperature. The obtained catalysts were characterized by XRD, TEM and EDS. From the EDS, the atom % ratio of the Pt-Pd/MWCNTs was found to be 50:50. From TEM results the Pt-Pd particle size was found to be 9.2 $\pm$3.3 nm. The TEM image is given in Figure 2.23.

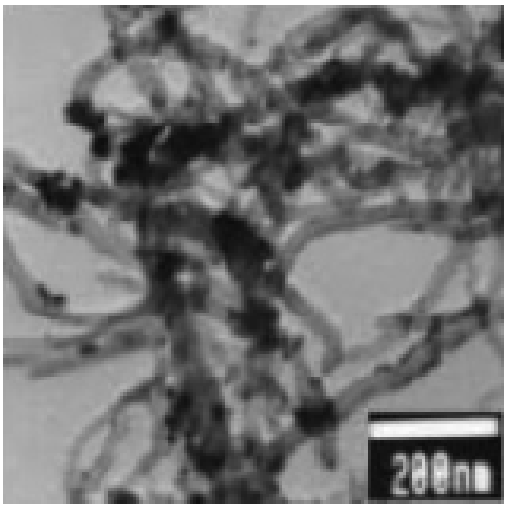


**Figure 2.23:** The TEM image of the Pt-Pd/MWCNTs [45].

In this thesis, preparation of carbon supported Pt-Pd bimetallic nanoparticles by $scCO_2$ deposition was investigated. Two methods were utilized for preparation and their results were compared. The schematic diagram of the preparation by first method is given in Figure 2.24. The first is the common method consisting in the deposition of the nonprecious metal (Pd) on a previously formed carbon-supported Pt. This method consists of two steps. In the first step the substrate is firstly exposed to the first organometallic precursor (OM-A ($PtMe_2COD$ for our case)) dissolved in $scCO_2$. After the adsorption of OM-A on the substrate at desired temperature and pressure, the vessel is depressurized. Afterwards, OM-A adsorbed on the substrate is reduced to its metal form by chemical reduction under $H_2/N_2$ at atmospheric pressure and desired temperature. At the end of the reduction process M-A/Substrate is obtained. In the second step; previously formed M-A/Substrate is exposed to the second organometallic precursor (OM-B ($Pd(acac)_2$ for our case) which is dissolved in $scCO_2$. After the adsorption of OM-B on the M-A/Substrate is completed at desired temperature and pressure, chemical reduction in $scCO_2$ with $H_2$ is done at the same temperature with the adsorption of OM-B on the M-A/Substrate but at higher pressure than that of adsorption since injection of $H_2$ into the system requires higher

pressure values. Then the system is depressurized and the M-A - M-B supported catalysts are obtained.

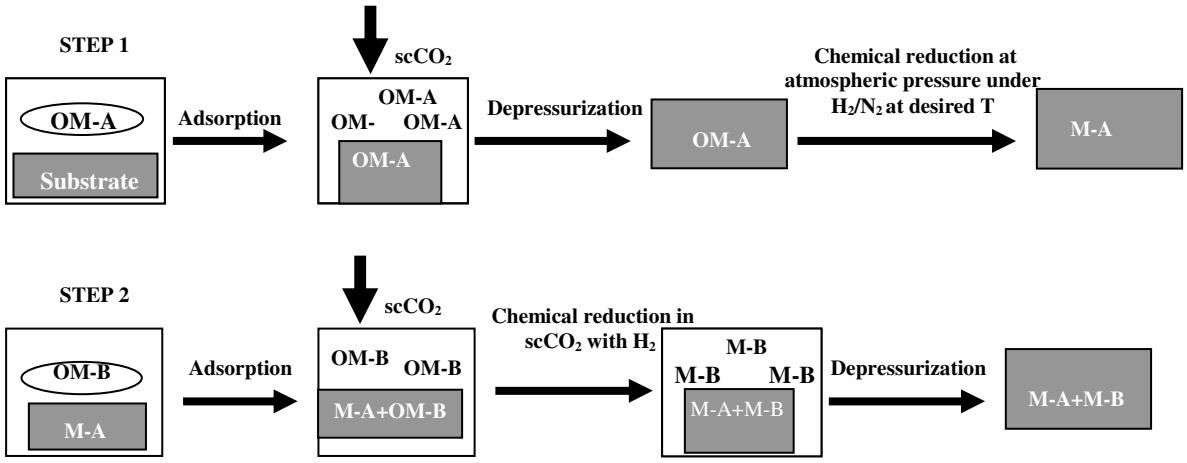


**Figure 2.24:** Schematic representation of method 1 for Pt-Pd/BP 2000 preparation. (OM-A: $Pt(cod)me_2$, OM-B: $Pd(acac)_2$).

In the second method which is represented in Figure 2.25; the substrate is exposed to the organometallic precursors; OM-A ($PtMe_2COD$) and OM-B ($Pd(acac)_2$) dissolved in $scCO_2$, simultaneously. After the adsorption of both of the organometallic precursors on the substrate at desired temperature and pressure, chemical reduction in $scCO_2$ with $H_2$ is accomplished at the same temperature as the adsorption temperature and at a higher pressure than the adsorption pressure due to the same reason explained in the first method. Finally, the system is depressurized and the bimetallic M-A - M-B supported catalysts are obtained.

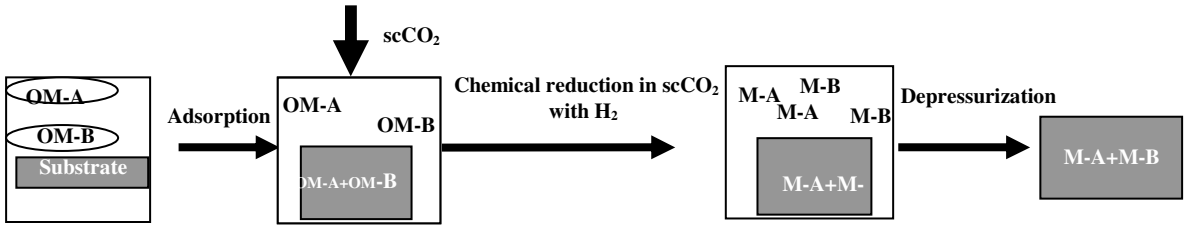


**Figure 2.25:** Schematic representation of method 2 for Pt-Pd/BP 2000 preparation. (OM-A: $Pt(cod)me_2$, OM-B: $Pd(acac)_2$).

# 3 EXPERIMENTAL SECTION

## 3.1 Materials

Palladium (II) acetylacetonate (99 %) was purchased from Aldrich. Dimethyl (cyclooctadiene) platinum (II) was purchased from STREM. Black Pearl 2000 was purchased from Cabot International. The chemicals were used as received. Carbon dioxide (99.998 %) was purchased from Messer Aligaz.

## 3.2 Experimental Methods

### 3.2.1 The adsorption isotherm experiments of $PtMe_2COD$ and $Pd(acac)_2$ on BP 2000 in $scCO_2$

The main reactor vessel used for adsorption and reduction experiments was a 54 mL stainless steel vessel which is fitted with two sapphire windows (1 in. in diameter, Sapphire Engineering, Inc., Pocasset, MA) sealed on both sides of the vessel with polyetheretherketone O-rings (Valco Instruments, Inc., Houston, TX), a thermocouple assembly, a vent line and a rapture disk assembly (Autoclave Engineers). The experimental set-up of the system is given in Figure 3.1. For the adsorption isotherm experiments, a certain amount of organometallic precursor (palladium (II) acetylacetonate) ($Pd(acac)_2$ or dimethyl cyclooctadiene platinum (II) ($PtMe_2COD$), a certain amount of substrate (black pearl 2000) in a pouch and a magnet were placed into the main reactor vessel at each run The vessel was heated to 60 $^oC$ by a circulating heater/cooler (Cole Parmer, Model 12108-15). Then it was pressurized with $CO_2$ from a syringe pump (Teledyne Isco, Model 260 D) to a pressure of 20 MPa. For the $Pd(acac)_2$ case, a yellow solution of fluid phase was observed from sapphire windows which indicated that the organometallic precursor was

dissolved in supercritical $CO_2$. In the case of $PtMe_2COD$, a colorless solution was observed. During the adsorption process, the organometallic precursors dissolved in the fluid phase adsorbed onto the substrate. The system was kept at 20 MPa and 60 $^oC$ in batch mode until equilibrium was reached which took around 4 hours for each run. Then, the solution in the vessel was drained slowly through the vent line into the hood. The vessel was cooled and the impregnated substrate was removed from the vessel. The amount of the organometallic precursors adsorbed onto the substrate was determined by the weight change of the substrate using an analytical balance accurate to ± 0.1 mg (AND GR-200).

### 3.2.2 The preparation of Pd/BP 2000 catalysts

For the preparation of Pd/BP 2000 catalysts, firstly $Pd(acac)_2$/BP 2000 composites were prepared in the main reactor vessel by placing predetermined amounts of $Pd(acac)_2$ and BP 2000 and charging the vessel with $scCO_2$ to a pressure of 20 MPa at the desired experimental temperature. The temperature selected for the adsorption of $Pd(acac)_2$ onto porous BP 2000 in $scCO_2$ was same with the desired reduction temperature at each run. The system was kept around 4 h at these conditions. A 10 mL solution of excess $H_2$ in $scCO_2$ ($P_{H2}$= 0.8 MPa, $P_{total}$= 27.6 MPa) was injected using the syringe pump. For the injection, first the 10 mL vessel which was placed between the main reactor vessel inlet and syringe pump was filled with $H_2$ at 0.8 MPa. Afterwards, $scCO_2$ was sent to the 10 ml vessel at a pressure of 27.6 MPa. Then excess $H_2$/$scCO_2$ mixture was injected inside the main reactor vessel containing the $Pd(acac)_2$/BP 2000 composites in $scCO_2$ solution at 20 MPa and selected reduction temperatures which were 50, 60, 70 and 80 $^0C$ at different runs. The adsorption and reduction pressure, substrate and organometallic amount put into the vessel were kept constant at each experiment for the investigation of the reduction temperature effect on Pd particle size growth. It was observed that, after a short time $H_2$ was injected, the yellow solution turned colorless which indicated that the organometallic precursor remaining in the solution was reduced as well as the adsorbed precursor on the Black Pearl 2000. After the reduction process, the vessel was depressurized slowly and allowed to cool down. The metal/substrate was taken away from the vessel. The metal loading of the composites was determined from the weight change by using an analytical

balance. For the investigation of the effect of Pd loading (wt.% metal), the above procedure for the adsorption and reduction experiments was carried out, but this time the adsorption and reduction temperature were kept constant at 80 $^0$C and the amount of $Pd(acac)_2$ put in the main reactor vessel was changed at each run.

### 3.2.3 Preparation of Pt/BP 2000 catalysts

In order to prepare Pt/BP2000 catalysts, a predetermined amount of $PtMe_2COD$ and BP2000 were put in the high pressure main reactor vessel. The vessel was heated to 80 $^0$C. Then, the vessel was filled with $CO_2$ up to 20 MPa by the syringe pump. $PtMe_2COD$ dissolved in $scCO_2$ and adsorbed on the surface of BP2000. After the system reached equilibrium, a 10 ml mixture of $H_2$ and $CO_2$ ($P_{H2}$= 0.8 MPa, $P_{total}$= 27.6 MPa) was injected into the vessel using the syringe pump as described above. Reduction was continued for 5 hours. Then, the vessel was drained and the system was cooled down. The metal loadings of the catalysts were calculated from the weight change by using an analytical balance.

### 3.2.4 Preparation of Pt-Pd/BP 2000 catalysts

For the preparation of the Pd-Pt/BP 2000 catalysts with different Pt/Pd molar ratios, two methods were followed. The first method involved the preparation of BP 2000 supported platinum followed by deposition of Pd on Pt/BP 2000. This method is divided into two steps. At the first step, predetermined amount of $PtMe_2COD$ and BP 2000 were put in the high pressure vessel which was then heated to 60 $^0$C. Then, the vessel was charged with $CO_2$ to 20 MPa by the help of a syringe pump. $PtMe_2COD$ dissolved in $scCO_2$ and adsorbed on the surface of BP 2000. The vessel was depressurized after the system reached equilibrium and allowed to cool down. The prepared $PtMe_2COD$/BP 2000 was then placed in an alumina process tube and reduced in a tubular furnace (Thermolyne 21100) at 200 $^0$C under flowing $H_2/N_2$ at 100 mL/min for 4 hours. The Pt loading was determined by using an analytical balance. At the second step, predetermined amount of $Pd(acac)_2$ and previously prepared Pt/BP 2000 were put in the high pressure main reactor vessel. The vessel was heated to 80 $^0$C followed by $scCO_2$ charging up to a pressure of 20 MPa. The system was kept overnight at these conditions. For reduction, a 10 mL solution

of excess $H_2$ in $scCO_2$ ($P_{H2}$= 0.8 MPa, $P_{total}$= 27.6 MPa) was injected using the syringe pump. For the injection, first the 10 mL vessel which was placed between the main reactor vessel inlet and syringe pump was filled with $H_2$ at 0.8 MPa. Afterwards, $scCO_2$ was sent to the 10 ml vessel at a pressure of 27.6 MPa. Then excess $H_2$/$scCO_2$ mixture was injected inside the main reactor vessel containing the Pt-Pd$(acac)_2$/BP 2000 composites in $scCO_2$ solution at 20 MPa and 80 $^0$C. Reduction was completed in 3 hours. After the reduction process, the vessel was depressurized slowly and allowed to cool down. The bimetallic particles/substrate was taken away from the vessel. The Pd loading of the Pt-Pd/BP 2000 was measured from the weight change by using an analytical balance.

In the second method, predetermined amount of Pd$(acac)_2$ and Pt$(cod)me_2$ were put in the high pressure main reactor vessel, simultaneously. The vessel was heated to 80 $^0$C and $scCO_2$ was charged inside at 20 MPa. When the system reached equilibrium around 6 hours, 10 mL solution of excess $H_2$ in $scCO_2$ ($P_{H2}$= 0.8 MPa, $P_{total}$= 27.6 MPa) was injected inside the vessel using the syringe pump. Reduction was completed in 5 hours. Then, the vessel was drained and the system was cooled down. The metal loading of the bimetallic catalysts were calculated from the weight change by using an analytical balance.

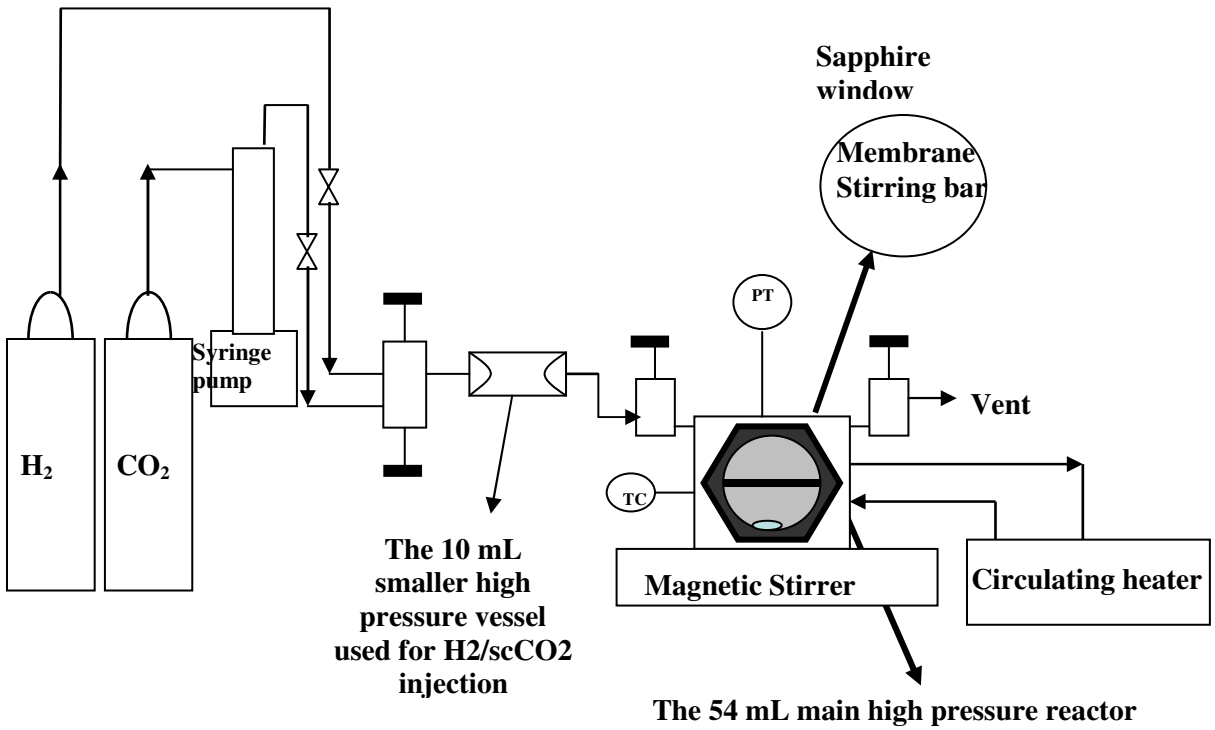


**Figure 3.1:** Schematic diagram of the experimental system.

### 3.3 Characterization

XRD continuous measurements were carried out by using Cu Kα source Huber G 670 Imaging Plate in a 2θ range of $5^0$- $86.915^0$ with a scanning rate of $5.5^0$ $min^{-1}$. The morphology of the supported catalysts was characterized by high-resolution transmission electron microscopy (TEM). Specimens for TEM examination were prepared by carefully crushing the samples with a mortar and pestle set. The resulting powders were suspended in a volatile solvent and ultrasonicated to obtain a uniform suspension. One or two drops of this suspension were deposited onto a copper mesh grid coated with a holey carbon film (Quantifoil Micro Tools GmbH). The TEM specimens were allowed to dry completely before examination in a JEOL 2010 FasTEM operating at 200 kV. This instrument is

equipped with a high-resolution objective lens pole-piece (spherical aberration coefficient Cs = 0.5mm) giving a point-to-point resolution of <0.19 nm in phase contrast images. Chemical microanalysis was performed *in situ* using an EDAX Phoenix atmospheric thin window energy-dispersive X-ray spectrometer (EDS).

### 3.3.1 Characterization with EDS

Energy dispersive X-ray spectroscopy (EDS) is an analytical technique which is used for the elemental analysis or chemical characterization of a sample. Its characterization is due to the fundamental principle that each element has a unique atomic structure which allows x-rays that are characteristic of an element's atomic structure. For characterization, a high energy beam of charged particles such as electrons or protons or a beam of X-rays is focused into the sample studied. An atom within the sample contains unexcited (ground state) electrons in electron shells bound to nucleus. The focused high energy beam may excite an electron in an inner shell ejecting it form the shell while creating an electron hole where the electron was [46]. In other words, in order to return the atom to its normal state an electron from an outer atomic shell drops into the vacancy in the inner shell. This drop results in the loss of a specific amount of energy which is the difference between the vacant shell and the shell contributing the electron. This energy is in the form of electromagnetic radiation x-rays. Since the energy levels in all the elements are different, element-specific or characteristic x-rays are generated. EDS uses detection equipment in order to measure the energy values of these characteristic x-rays which are generated. By using a semiconductor material to detect the x-rays and a multichannel analyzer, an x-ray microanalysis system converts x-ray energy into an electronic count. The accumulation of these energy counts creates a spectrum which represents the chemical analysis of the sample. Since the energy of the X-rays are characteristic of the difference in energy between the two shells and of the atomic structures of the element from which they are emitted, this allows the elemental composition of the sample to be measured [47].

# 4 RESULTS & DISCUSSION

## 4.1 The adsorption isotherms and the kinetics model development

In this thesis, the adsorption isotherms of $PtMe_2COD$ and $Pd(acac)_2$ on BP2000 in $scCO_2$ were determined at 20 MPa and 60 $^0$C. There are marked differences between the two isotherms. The adsorption isotherm for the $Pd(acac)_2$-BP2000-$scCO_2$ system is linear whereas the isotherm for the $PtMe_2COD$-BP2000-$scCO_2$ system is non-linear. The adsorption isotherm for the $Pd(acac)_2$-BP2000-$scCO_2$ system is given in Figure 4.1.

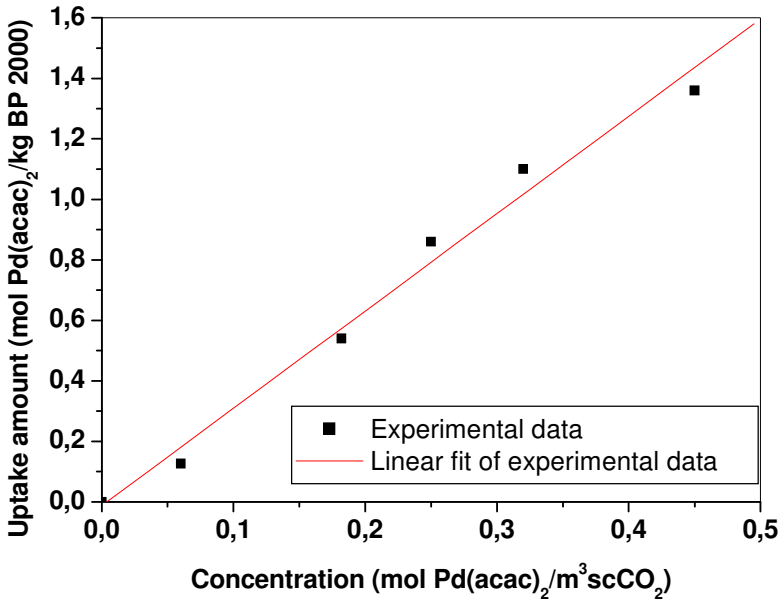


**Figure 4.1:** The experimental data and the linear fit for the adsorption isotherm of Pd(acac)2-BP 2000-scCO2 system at 20 MPa and 60 $^0$C.

From Figure 4.1, the relation between the uptake amount of organometallic precursor ($Pd(acac)_2$) (denoted by C) on substrate (q (mol OM/kg BP 2000)) and the concentration in supercritical phase (C (mol OM/$m^3$ $scCO_2$)) is given from the slope of the linear fit to the experimental data in equation (4.1):

$$q = 3.22\ C \qquad \textbf{(4.1)}$$

The adsorption isotherm for the $PtMe_2COD$-BP2000-$scCO_2$ system is non-linear and can be represented by the Langmuir model given by:

$$q = \frac{K_1 Q_0 C}{1 + K_1 C} \qquad \textbf{(4.2)}$$

Where; $K_1$ is the Langmuir adsorption constant ($m^3$ $scCO_2$/mol OM) and $Q_0$ is the adsorption capacity (mol OM/kg substrate), $K_1Q_0$ is the relative affinity of the OM towards the surface of the adsorbent. Using non-linear regression analysis, $K_1 = 0.14$ and $Q_0 = 4.5$. The experimental data of the adsorption isotherm at 20 MPa and 60 $^0$C was fitted to Langmuir model after finding the model constants, given in Figure 4.2 The fitting error of the model to the experimental data was found to be 15%.

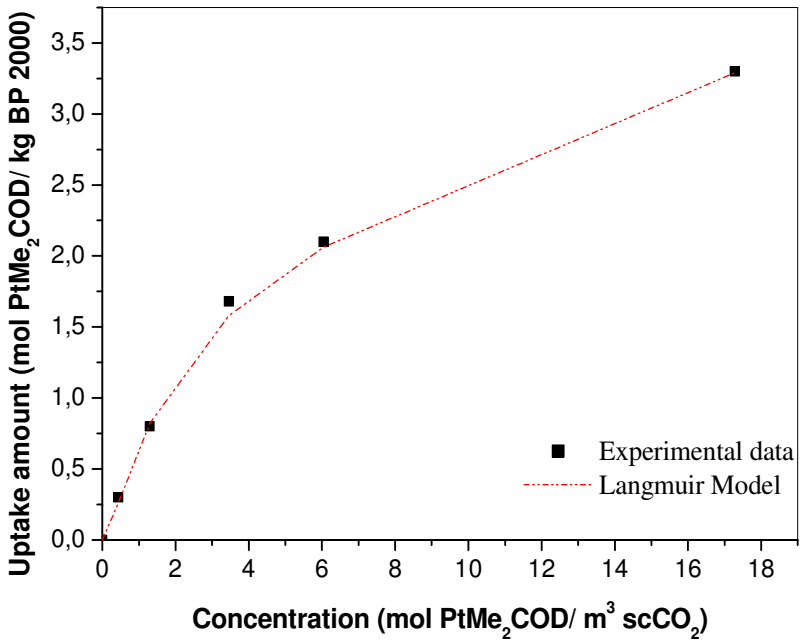


**Figure 4.2:** Experimental data and Langmuir Model fit for the adsorption isotherm of PtMe2COD-BP 2000-scCO2 system at 20 MPa and 60 $^{0}$C.

This difference between the adsorption isotherms can most likely be attributed to substantially higher concentrations of $PtMe_2COD$ in the $scCO_2$ phase. In the isotherms, the upper limit of the concentration in the fluid phase corresponds to the solubility of the organometallic precursor in the fluid phase. Since the solubility of $PtMe_2COD$ in $scCO_2$ ($21.7\ mol/m^3$) is much higher than the solubility of $Pd(acac)_2$ in $scCO_2$ ($0.66\ mol/m^3$) at 20 MPa and 60 $^{o}$C [39], the range of concentration of $PtMe_2COD$ in the fluid phase is much larger. The area covered by $PtMe_2COD$ or $Pd(acac)_2$ molecules on the BP2000 surface, $S_A$, can be calculated using:

$$S_A = Q_o A \pi r^2 \qquad \textbf{(4.3)}$$

where, $Q_o$ is the maximum uptake, A is Avogadro's number and r is the radius of a $PtMe_2COD$ or $Pd(acac)_2$ molecule. The diameters of $Pd(acac)_2$ and $PtMe_2COD$ molecules were determined using the Marvin Beans software as 0.80 and 0.55 nm, respectively. The area covered by $PtMe_2COD$ molecules is 620 $m^2/g$ whereas the area covered by $Pd(acac)_2$ molecules is 640 $m^2/g$. This indicates that, at maximum uptake, both $PtMe_2COD$ and $Pd(acac)_2$ molecules cover all of the accessible surface of the BP 2000. The uptake amount of $Pd(acac)_2$ on BP 2000 is higher than the uptake amount of $PtMe_2COD$ at the same fluid concentration in the supercritical phase, indicative of a stronger precursor-support interaction for $Pd(acac)_2$-BP2000.

Recently, we investigated the thermodynamics and kinetics of adsorption of bis(2,2,6,6-tetramethyl-3,5-heptanedionato) (1,5-cyclooctadiene) ruthenium (II) from $scCO_2$ onto carbon aerogel [19]. Similar to the model given in that study, a kinetics model was developed for the $Pd(acac)_2$-$scCO_2$-BP 2000 system taking into account the pore diffusion and local equilibrium in the pores of BP 2000. Four steps were identified for adsorption from the supercritical phase. These steps were mass transfer of adsorbate from the supercritical fluid phase to the adsorbent, supercritical diffusion in the pores of the adsorbent, adsorption onto the surface of adsorbent and surface diffusion within the adsorbent, respectively. The first step, which is the mass transfer of $Pd(acac)_2$ from $scCO_2$ phase to the BP 2000 is best described by film diffusion which depends on the concentration difference of the bulk $scCO_2$ phase and surface of BP 2000. Since the solutions were well stirred and perfectly mixed in the experiments, it was assumed that the concentration of $Pd(acac)_2$ at the bulk $scCO_2$ and BP 2000 surface were equal. Therefore, the effect of film diffusion was neglected. The second step which is supercritical $CO_2$ dissolved organometallic diffusion into the pores of BP 2000 can be best described by the Fick's first law which is given by equation (4.4):

$$(N_A)_e: -D_e \frac{\partial C_A}{\partial r} \qquad \textbf{(4.4)}$$

In Equation (4.4), $(N_A)_e$ (mol/m$^2$s) is the diffusion flux of the organometallic precursor dissolved in supercritical carbon dioxide to the porous volume in the carbon substrate. $D_e$ is the effective diffusivity for diffusion in pores given in m$^2$/s. The pores in the pellet are not straight and cylindirical; rather they are a series of tortuous, interconnecting paths of pore bodies and pore throats with varying cross-sectional areas [48]. The optimum model to evaluate the effective diffusivity is the one which represents the geometry of the void space complexity with easily measurable properties of the catalyst pellet. A model that takes into account the surface area, pore volume per gram and density of the solid phase in order to obtain the effective diffusion [49] is given by equation (4.5):

$$D_e = \frac{\varepsilon_p D}{\tau} \qquad \textbf{(4.5)}$$

where $\varepsilon_p$ is the porous solid porosity, D is the diffusivity in case of bulk diffusion in the absence of surface diffusion, $\tau$ is the tortuosity of the pores which is an adjustable parameter varying from less than unity to more than 6 depending on experimental data for various catalysts [49]. Tortuosity is defined as the ratio of the actual distance of a molecule that travels between two points to the shortest distance between those two points [48]. For our system D is represented by $D_{AB}$ which is the binary diffusion coefficient in supercritical fluids (A denotes the organometallic precursor $Pd(acac)_2$, B denotes the supercritical $CO_2$ in this study). Also, for systems where the molecular size of the solute approaches the pore size, a reduction in diffusivity is observed. This can be quantified with a size restriction factor $F(\lambda)$ which depends on the ratio of the solute diameter to the pore size [50]. When equation (4.5) is modified taking into account the binary diffusion coefficient in supercritical fluid and size restriction factor; effective diffusvity correlation becomes:

$$D_e = F(\lambda) \frac{D_{AB} \varepsilon_p}{\tau} \qquad \textbf{(4.6)}$$

The size restriction factor $F(\lambda)$ can be estimated from the Chantong equation [50];

$$F(\lambda)= 1.03\ e^{-4.5\lambda} \quad \textbf{(4.7)}$$

where λ is the ratio of the solute diameter (ds) to pore size (dp). Solute diameter of $Pd(acac)_2$ molecule is 0.8 nm, the average pore size of the BP 2000 carbon black samples was taken as 20 nm from Figure 4.3 which is based on the volumetric sorption analysis study by Kruk et al. [51].

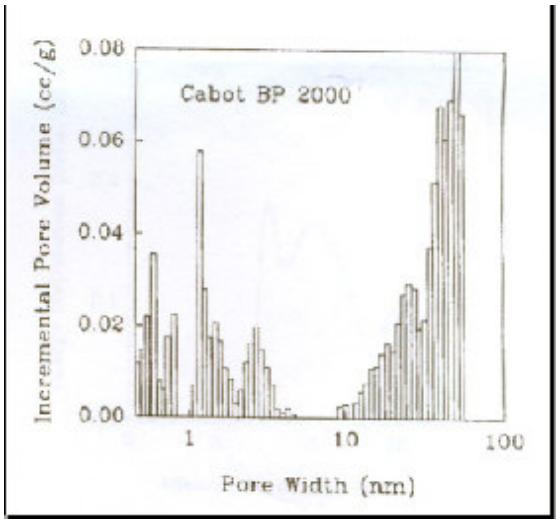


**Figure 4.3:** The pore volume distribution for the carbon black (Black Pearl 2000) sample [51]**.**

In order to estimate the binary diffusion coefficient, the Schmidt number correlation proposed by Funazukuri et al. [52] was used. This correlation is a method used to calculate binary diffusion coefficients for various organic compounds in supercritical fluids. The correlation is given in equation (4.8):

$$Sc^{+}= \frac{Sc}{Sc^{*}} = 1 + \exp\left[\sum_{i=0}^{5} a_i \left(\frac{v_0}{v}\right)^i\right] \quad \textbf{(4.8)}$$

For binary diffusion;

$$Sc^{*} = \frac{5}{6}\left[\frac{\sigma_1 + \sigma_2}{2\sigma_2}\right]^2\left[\frac{2M_1}{M_1 + M_2}\right]^{1/2} \quad \textbf{(4.9)}$$

In the above equations, Sc is the Schmidt number at high pressure and $Sc^{*}$ is the Schmidt number at atmospheric pressure. $Sc^{+}$ is the ratio of the Schmidt number at high pressure to that at atmospheric pressure. Moreover, $v_0$ is the hard-sphere-closest-packed volume of solvent molecules, v is molar volume of solvent, $\sigma_1$ and $\sigma_2$ are the hard sphere diameters and $M_1$ and $M_2$ are the molecular weights of the solute and solvent respectively ($Pd(acac)_2$ and $CO_2$ in our study). Hard-sphere-closest-packed volume is a polynomial function of temperature [52] given by equation (4.10):

$$v_0 = \frac{1}{1.384}\left(\sum_{i=0}^{4} c_i T^i\right) \quad \textbf{(4.10)}$$

In order to solve equations (4.8)-(4.10), the unknown constants $a_i$ and $c_i$ should also be determined. These are constants for correlation of Schmidt number with solvent molar volume and effective hard-sphere packed volume, respectively. These constants are given in Table 4.1.

**Table 4.1:** The constants for correlation of Schmidt number with solvent molar volume ($a_i$) and effective hard-sphere packed volume ($c_i$) [52]**.**

| I | $a_i$ | $c_i$ |
|---|---|---|
| 0 | -4.92519817 | $4.452 \times 10^{-5}$ |
| 1 | 54.5529385 | $-1.152 \times 10^{-7}$ |
| 2 | -245.231443 | $2.749 \times 10^{-10}$ |
| 3 | 607.893924 | $-3.073 \times 10^{-13}$ |
| 4 | -708.884016 | $1.290 \times 10^{-16}$ |
| 5 | 329.611433 | - |

Taking into account the constants in Table 4.1 and the other parameters in equations (4.8)-(4.10), Sc was evaluated. The parameters used in the solution of these equations and results are given in Table 4.2.

**Table 4.2:** Parameters and results of Schmidt number correlation

| | | |
|---|---|---|
| $v_0$ | Hard sphere closest packed volume of $CO_2$ at 333 K | $1.94 \times 10^{-5}$ $m^3$/mol |
| v | Molar volume of $CO_2$ | $6.190 \times 10^{-5}$ $m^3$/mol [23] |
| $\sigma_1$ | Hard sphere diameter of $Pd(acac)_2$ | 0.8 nm |
| $\sigma_2$ | Hard sphere diameter of $CO_2$ | 0.3996 nm [53] |
| $M_1$ | Molecular weight of $Pd(acac)_2$ | 304.64 g/mol |
| $M_2$ | Molecular weight of $CO_2$ | 44 g/mol |
| $Sc^*$ | Schmidt number at atmospheric pressure | 2.48199 |
| $Sc^+$ | Schmidt number ratio at high pressure to atmospheric pressure | 2 |
| Sc | Schmidt number | 4.96 |

After finding the Schmidt number with the help of the correlation proposed by Funazukuri et al. [52], the binary diffusion coefficient for the $Pd(acac)_2$–BP2000-$scCO_2$ system was calculated using:

$$Sc = \frac{\upsilon}{\rho \times D_{AB}} \quad \textbf{(4.11)}$$

In equation (4.11), the binary diffusion coefficient ($D_{AB}$) was calculated by substituting the Sc number as 4.96, and viscosity and density of $CO_2$ at 20 MPa and 60 $^0$C as 6.3 cP and 724 kg/$m^3$, respectively. $D_{AB}$ was calculated as $1.72 \times 10^{-8}$ $m^2$/s.

The third step for the adsorption model development is the adsorption onto the surface of carbon. Local equilibrium was assumed for the adsorption experiments where the adsorbed phase concentration was related to the $scCO_2$ concentration through the adsorption isotherm. The final step which is surface diffusion within the adsorbent was neglected since there was a strong adsorption bond between the solute and the substrate and the migration of the precursor along the concentration gradient in the adsorbed phase was neglected. So,

the adsorption kinetics model was developed according to steps 2 and 3, taking into account the diffusion of $Pd(acac)_2$ dissolved in $scCO_2$ into the porous spherical BP2000 pellets. In order to develop a model for the investigation of kinetics of adsorption of $Pd(acac)_2$ onto spherical BP2000 pellets at the given experimental conditions (20 MPa, 60 $^0$C), a shell balance represented in Figure 4.4. was done to describe the unsteady state adsorption process. The equation derived is given in Equation (4.12).

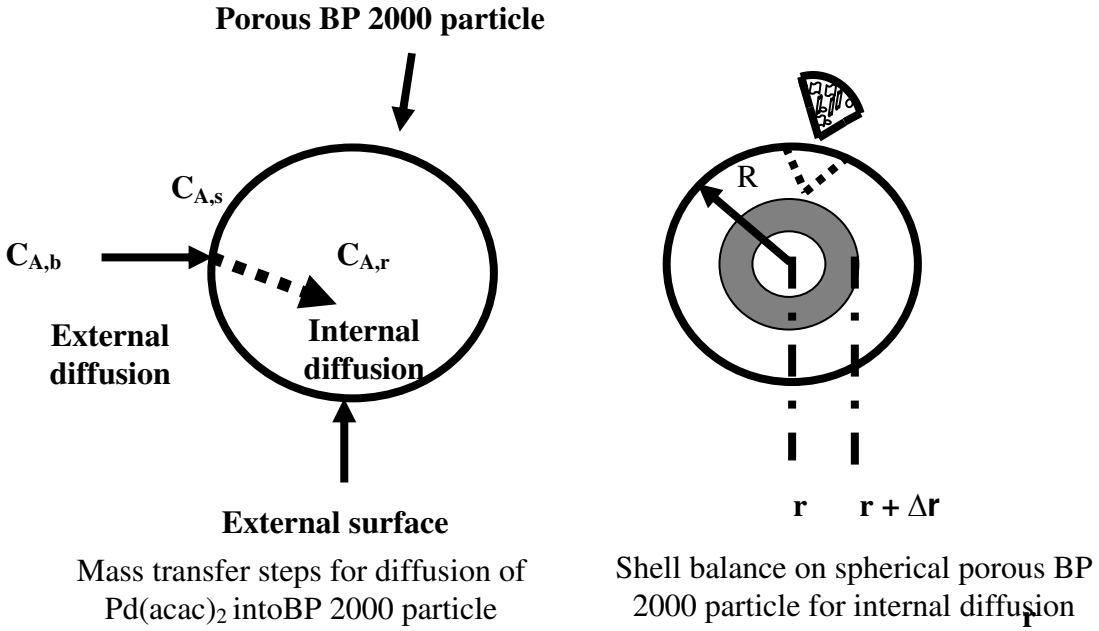


Mass transfer steps for diffusion of $Pd(acac)_2$ intoBP 2000 particle

Shell balance on spherical porous BP 2000 particle for internal diffusion

**Figure 4.4:** Representation of mass transfer steps and shell balance for diffusion of Pd(acac)2 into BP 2000.

$$\varepsilon_p \frac{\partial C_A}{\partial t} + \rho_p \frac{\partial q}{\partial t} = D_e \left( \frac{\partial^2 C_A}{\partial r^2} + \frac{2}{r} \frac{\partial C_A}{\partial r} \right) \qquad \textbf{(4.12)}$$

In equation (4.12), $C_A$ is the concentration of $Pd(acac)_2$ in $scCO_2$ (mol/$m^3$), q is the uptake amount of $Pd(acac)_2$ on BP2000 (mol/kg) and t is the time (s). The term $\frac{\partial C_A}{\partial t}$ represents the accumulation term, $\frac{\partial q}{\partial t}$ represents the adsorption term and $\frac{\partial C_A}{\partial r}$ represents the flux term. The boundary conditions are;

Boundary Condition-1: $\frac{\partial C_A}{\partial r} = 0$ at r= 0

Boundary Condition-2: - V $\frac{\partial C_A}{\partial t} = m\ S\ D_e \frac{\partial C_A}{\partial r}$ at r= R

where, V is the volume of $scCO_2$ (high pressure vessel), m is the mass and S is the external surface area of BP2000 particles, respectively. The initial conditions for equation 10 are;

Initial Condition-1: $C_A = 0$ at t= 0 at $0 \le r < R$

Initial Condition-2: $C_A = C_{A0}$ at t= 0 at r= R

Equation (4.12) was modified by substituting the isotherm relation for the accumulation term and using the chain rule and the following equation was obtained;

$$\frac{\partial C_A}{\partial t} = \frac{D_e}{\varepsilon_p + \rho_p (\frac{\partial q}{\partial C_A})} (\frac{\partial^2 C_A}{\partial r^2} + \frac{2}{r}\frac{\partial C_A}{\partial r}) \quad \textbf{(4.13)}$$

With the given boundary and initial conditions, Equation 4.13 was converted to a set of ordinary differential equations using numerical method of lines method and solved in Polymath program substituting the values of the parameters given in Table 4.3.

**Table 4.3:** Parameters used in the solution of adsorption kinetics model

| | ***Parameters*** | ***Definiton*** | ***Unit*** | Value |
|---|---|---|---|---|
| **BP 2000** | $\rho_P$ | Density of the porous carbon particles | $kg/m^3$ | 444 |
| | **R** | Radius of the spherical carbon particles | m | $6.5 \times 10^{-4}$ |
| | $\varepsilon_p$ | Porosity | - | 0.78 |
| | **m** | Mass of carbon used in experiments | kg | $10^{-4}$ |
| | **S** | External surface area per mass of carbon particles | $m^2/kg$ | 10.38 |
| | $\tau$ | Tortuosity-the adjustable parameter of the system | - | Varying from less than unity to more than 6 |
| **Bulk $scCO_2$properties** | **V** | Volume of $scCO_2$ (volume of high pressure vessel) | $m^3$ | $54 \times 10^{-6}$ |
| | $C_{A0}$ | Initial concentration of $Pd(acac)_2$ in $scCO_2$ at t=0 | $mol/m^3$ | 1.22 |
| **Slope of the isotherm** | **-** | $q/C_A$ | - | 3.22 |
| **Diffusivity** | $D_{AB}$ | Binary diffusion coefficient | $m^2/s$ | $1.72 \times 10^{-8}$ |
| | $d_s$ | $Pd(acac)_2$diameter | m | $8 \times 10^{-10}$ |
| | $d_p$ | Average pore size of carbon particle | m | $2 \times 10^{-9}$ |
| | $D_e$ | Effective diffusivity | $m^2/s$ | $1.77 \times 10^{-9}$ |

With the solution of Equation (4.13), the kinetics of adsorption was predicted which is shown in Figure 4.5. The adjustable parameter tortuosity was taken as 1.29 which is 1/εp [49]. There is very good agreement between the experimental data and the model with a fitting error of 5.6 %. As can be seen from Figure 4.5, it takes around 4 hours for the system to reach equilibrium determined from the adsorption kinetics model.

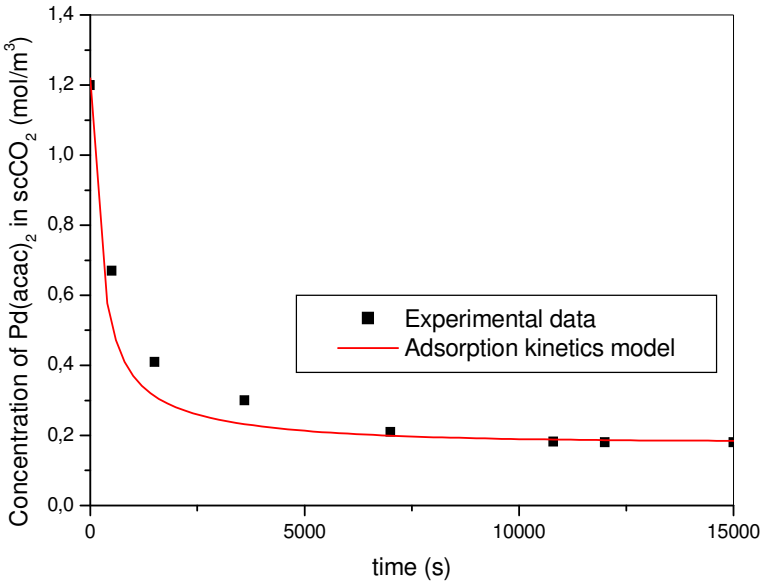


**Figure 4.5:** Experimental data and adsorption kinetics model solved for tortuosity value of 1.29.

The effect of the adjustable parameter 'tortuosity' on the adsorption kinetics was investigated. As can be seen in Figure 4.6, as tortuosity decreases it takes shorter time to reach equilibrium but the equilibrium concentration remains the same which is 0.183 $mol/m^3$.

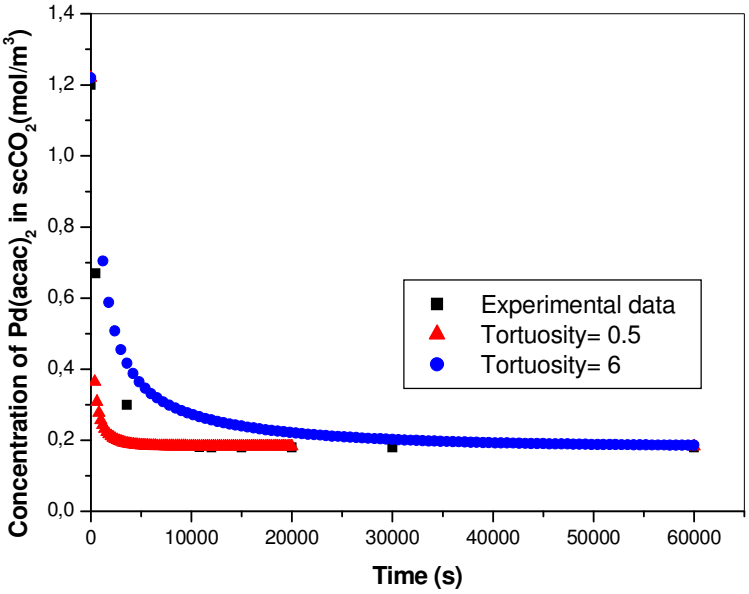


**Figure 4.6**: The effect of tortuosity factor on the adsorption kinetics.

The effect of another important factor which is substrate particle size on the adsorption kinetics was also investigated. As can be seen in Figure 4.7, as the particle size increases the time to reach equilibrium also increases.

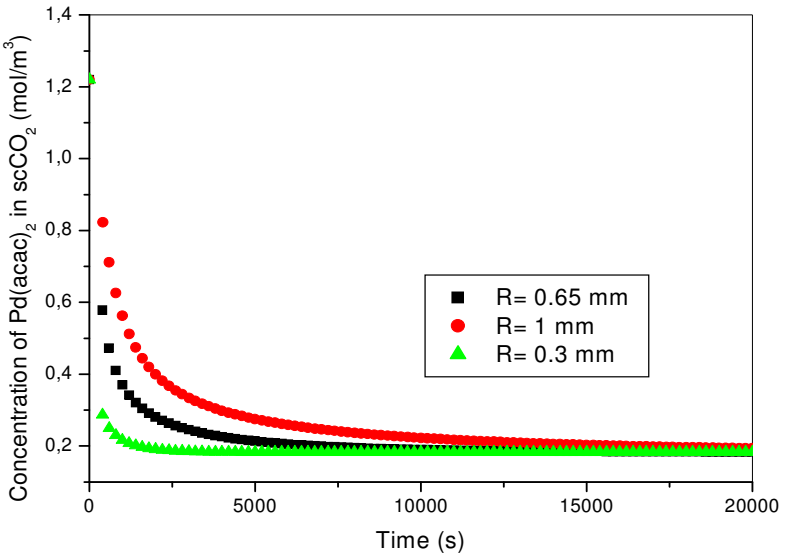


**Figure 4.7:** The effect of substrate particle size on the adsorption kinetics at a fixed tortosity value of 1.29.

Isotherm parameters have a great role on the prediction of adsorption kinetics. Since the solubility of $Pd(acac)_2$ in $scCO_2$ is quite low, the concentration range studied in the experiments is limited and a linear adsorption isotherm behavior is observed with a constant slope of 3.22. As seen in Figure 4.8, as the slope of isotherm increases from 3.22, to 9, the equilibrium concentration of solution decreases from 0.183 mol/$m^3$ to 0.08 mol/$m^3$; whereas it increases to 0.442 mol/$m^3$ when the isotherm slope decreases from 3.22 to 1.

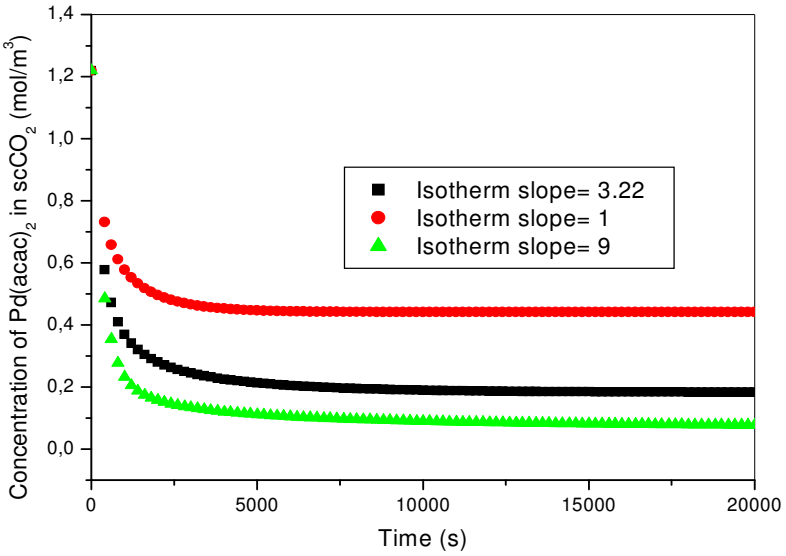


**Figure 4.8:** The effect of linear adsorption isotherm slope on the adsorption kinetics at a fixed tortuosity value of 1.29.

## 4.2 Preparation and characterization of Pd/BP 2000 catalysts

Pd/BP 2000 catalysts were prepared at different reduction temperatures and different metal loadings. The effect of reduction temperature and metal loading on the Pd particle size growth was investigated. It was found that reduction of the $Pd(acac)_2$ precursor could be carried out by subjecting the $Pd(acac)_2$/BP2000 to a supercritical mixture of $H_2$ and $CO_2$. Before the injection of hydrogen to the system, $Pd(acac)_2$ is distributed between the $scCO_2$ phase and the BP2000 phase. The yellow colored solution with dissolved $Pd(acac)_2$ turned colorless a short time after $H_2$ was injected as observed from the sapphire window on the side of the vessel. When the contents of the vessel were kept in $scCO_2$ at 80 $^0$C without any hydrogen, the color of the solution did not change and remained yellow for a prolonged period. The peaks for Pd in XRD spectra obtained from the catalysts indicated

that chemical reduction of adsorbed $Pd(acac)_2$ was also occurring on the surface of BP2000.

The effects of reduction temperature and metal loading on the average Pd particle size were investigated using XRD. Four different reduction temperatures of 50, 60, 70 and 80 $^0$C were selected. The XRD spectra obtained from the Pd/BP2000 catalysts with 20 wt. % Pd loading prepared at these four different reduction temperatures are given in Figure 4.9. The size of the Pd particles was obtained from the spectra using the Scherrer Formula which is expressed by equation 4.13.

$$d_{XRD} = \frac{0.9\,\lambda_w}{\beta_{1/2}\cos\theta} \qquad \textbf{(4.13)}$$

where $d_{XRD}$ is the average particle size (nm), $\lambda_w$ is the wavelength of X-ray (0.15406 nm), $\Theta$ is the angle at the peak maximum and $\beta_{1/2}$ is the width (radians) of the peak at half height. Since the characteristic { 1 1 1 } and { 2 0 0 } peaks overlap with the broad C peaks, the size of the Pd particles was calculated from the full width at half maximum of the {2 2 0} peak.

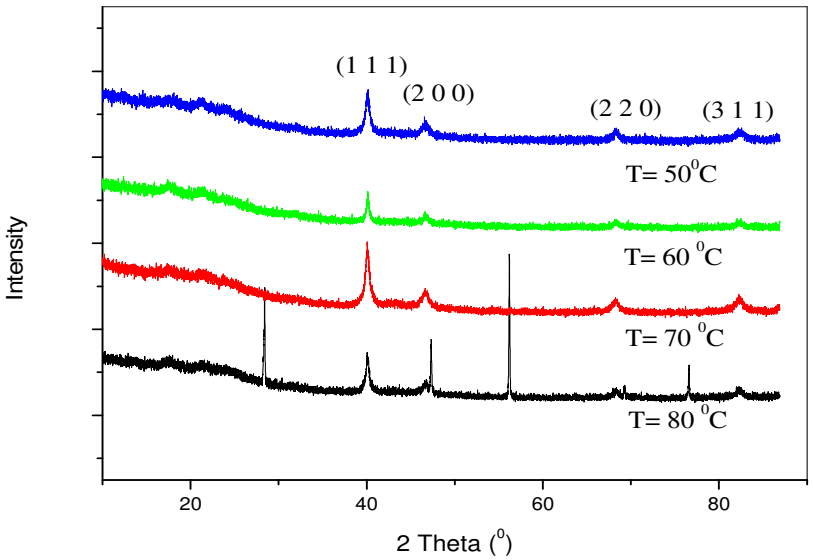


**Figure 4.9:** XRD spectra of the 20 wt.% Pd loaded samples prepared by chemical reduction in $H_2/scCO_2$ at different reduction temperatures.

As shown in Figure 4.10, the average Pd particle size increased as the chemical reduction temperature in $scCO_2$ was increased. The average size doubled from 7 nm to 14 nm as the temperature was increased from 50 to 80 $^{o}$C. The most likely explanation for this effect is an increase in the mobility of the reduced palladium atoms with increasing reduction temperature, which results in more extensive particle coarsening during the reduction process. In a study by Kim et al. [54] where $Pd(hfac)_2$ was deposited on $SiO_X$ in liquid $CO_2$ and reduced with $H_2$ at atmospheric pressure, it was found that the average Pd particle diameter increased from 5.9 nm to 7.9 nm when the reduction temperature was increased from 75 $^{0}$C to 150 $^{0}$C. The smaller Pd particle size obtained on SiOx can be attributed to the lower mobility of the Pd atoms on SiOx.

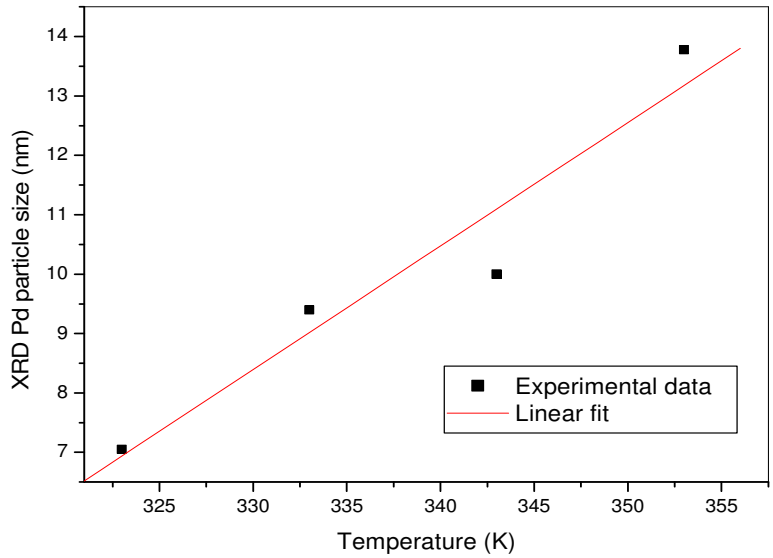


**Figure 4.10:** The effect of reduction temperature on the growth of Pd particles with XRD results shown in Figure 4.9.

Examples of TEM images obtained from the catalyst with 20 wt.% Pd loading prepared by chemical reduction in $H_2/scCO_2$ at 80 $^{0}$C are shown in Figure 4.11. Images such as

Figure 4.11.a., which were obtained at lower magnifications, reveal clearly the structure of the BP2000 support and the sizes and distribution of the Pd nano-particles. The lighter features in such images correspond to the support, which consists of inter-linked homogeneous C particles 20-50 nm in diameter as expected for BP2000. The darker features superimposed upon the support are the Pd nano-particles which are distributed rather inhomogeneously. These Pd nano-particles are present in a wide range of different sizes ranging from 3 nm up to around 100nm. Higher magnification images such as Figure 4.11.b. show that the C particles that comprise the support consist of disordered carbon. Moreover, such images reveal that the larger Pd nanoparticles (> 20 nm) have an irregular morphology suggesting that these may arise by the agglomeration of smaller nanoparticles migrating across the support surface instead of by coarsening due to the atomic diffusion of metallic Pd.

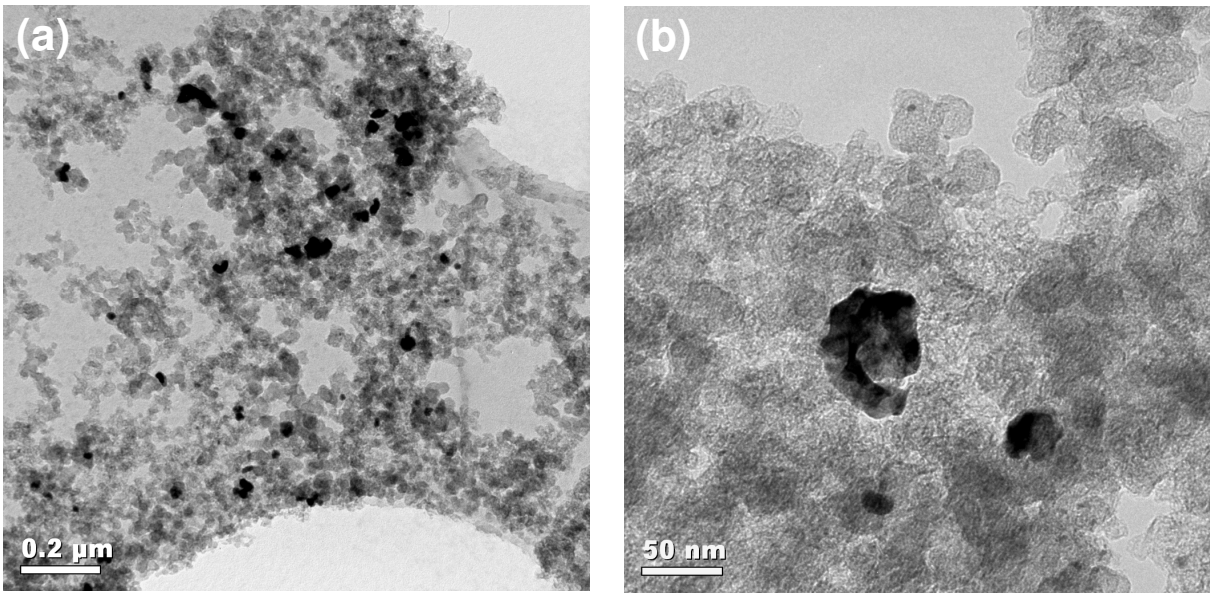


**Figure 4.11:** TEM images of the 20 wt.% metal loaded Pd/BP2000 catalysts prepared by chemical reduction in $H_2/scCO_2$ at 80 $^0$C.

The effect of metal loading on the growth of Pd particle size was also investigated. In these experiments, the chemical reduction was carried out at 80 $^0$C in $H_2/scCO_2$ ($P_{H2}$= 0.8 MPa, $P_{TOTAL}$= 27.6 MPa) and the amount of organometallic precursor put into the vessel before the adsorption experiments was varied. The amounts were selected based on the adsorption isotherm. The Pd loadings of the prepared catalysts were 3, 5, 12 and 20 wt. %. XRD spectra obtained from the catalysts with different Pd loadings are presented in Figure 4.12.

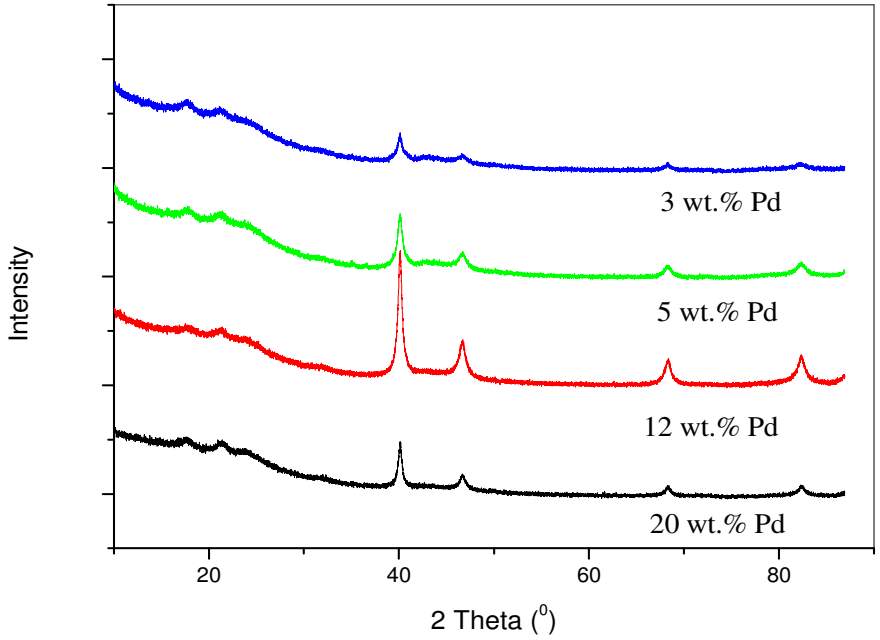


**Figure 4.12:** XRD patterns of Pd/BP2000 catalysts prepared by chemical reduction in $H_2/scCO_2$ at 80 $^0$C.

As can be seen in Figure 4.13, the average Pd particle size increased with the metal loading of the Pd/BP2000 composites: the average size increased from 7.8 nm to 14 nm as the loading was increased from 3 to 20 wt. % Pd.

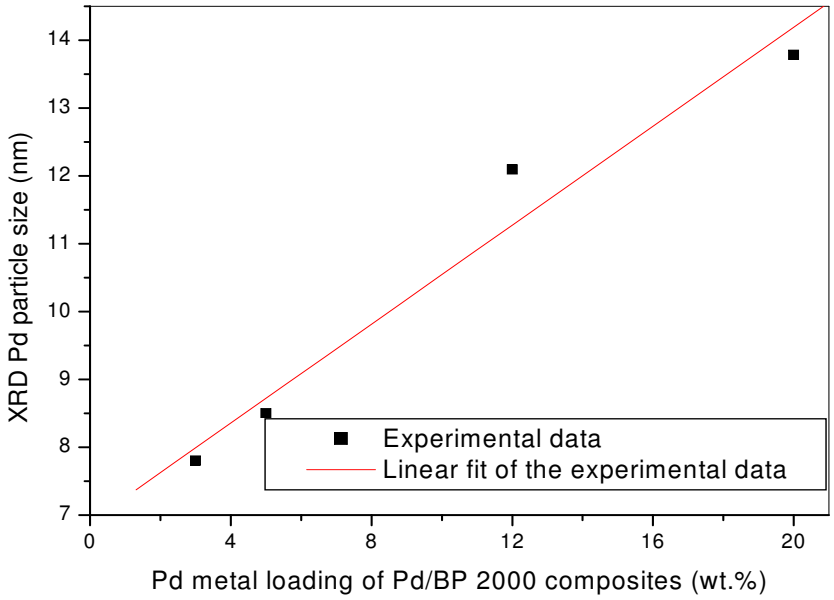


**Figure 4.13:** The effect of metal loading on the size of the particles from XRD results shown in Figure 4.12.

Ye et al. [17] decorated functionalized MWCNTs with Pd nanoparticles by supercritical deposition using $Pd(hfa)_2.xH_2O$ (hfa: hexafluoroacetylacetonate) as the precursor. The reduction was carried out in a $H_2/scCO_2$ mixture at 80 $^0$C. TEM images of the Pd/MWCNTs revealed well dispersed and spherical particles that were anchored onto the external walls of MWCNTs and the size of these particles were about 5-10 nm at a 10 wt.% Pd loading. In comparison, the TEM image of a commercial Pd/activated carbon with the same metal loading showed the existence of very large Pd particles that were irregularly distributed on the activated carbon surface. The surface of the BP 2000 support used in this

study seems to be similar in nature to the surface of activated carbon for the formation of Pd nanoparticles by supercritical deposition. As seen from the TEM images in Figure 4.11, the Pd particles are not homogeneously distributed and there are some very large particles on the BP2000 support. The summary of the average XRD Pd particle sizes of the Pd/BP 2000 catalysts prepared with different metal loadings and different reduction temperatures is given in Table 4.4.

**Table 4.4:** Summary of the average XRD Pd particle size of Pd/BP 2000 samples prepared with different metal loadings and reduction temperatures.

| Pd/BP 2000 sample number | Metal loading of the sample (wt.% of Pd/(Pd+BP2000) | Reduction temperature of the sample ($^0$C) | Pd average particle size from XRD measurement (nm) |
|---|---|---|---|
| 1 | 20 | 50 | 7.1 |
| 2 | 20 | 60 | 9.6 |
| 3 | 20 | 70 | 10 |
| 4 | 20 | 80 | 13.8 |
| 5 | 3 | 80 | 7.8 |
| 6 | 5 | 80 | 8.5 |
| 7 | 12 | 80 | 12.1 |

## 4.3 Preparation and characterization of Pt/BP 2000 catalysts

12 wt.% metal loaded Pt/BP2000 catalysts were prepared first by adsorption of a certain amount of $PtMe_2COD$ onto BP2000 from $scCO_2$ at 20 MPa and 80 $^0$C. Subsequently, the reduction of the prepared $PtMe_2COD$/BP2000 composites was carried out in $H_2/scCO_2$. The XRD data obtained from the Pt/BP2000 catalysts revealed a much finer distribution of metal than that for the Pd/BP2000 catalysts, with a mean particle size of 2 nm. This is consistent with the TEM data and representative images are shown in Figure 4.14. The particles are too fine to be observed in images obtained at lower magnifications (such as that used in Figure 4.11.) and high magnification images (e.g. Figure 4.14 : (a)) reveal a very uniform dispersion of metal nanoparticles with a narrow size distribution. The size and morphology of the Pt nanoparticles are revealed more

clearly in images obtained at even higher magnifications (e.g. Figure 4.14 : (b)). These nanoparticles are equiaxed and range from 2 to 4 nm in diameter. While there is some suggestion of agglomeration in these images, tilting experiments in the TEM have shown that this is mainly a projection artifact and that the vast majority of the Pt nanoparticles are well separated. These results indicate that the mobilities of the Pt atoms and nanoparticles on the BP2000 surface are significantly lower than the corresponding mobilities for Pd.

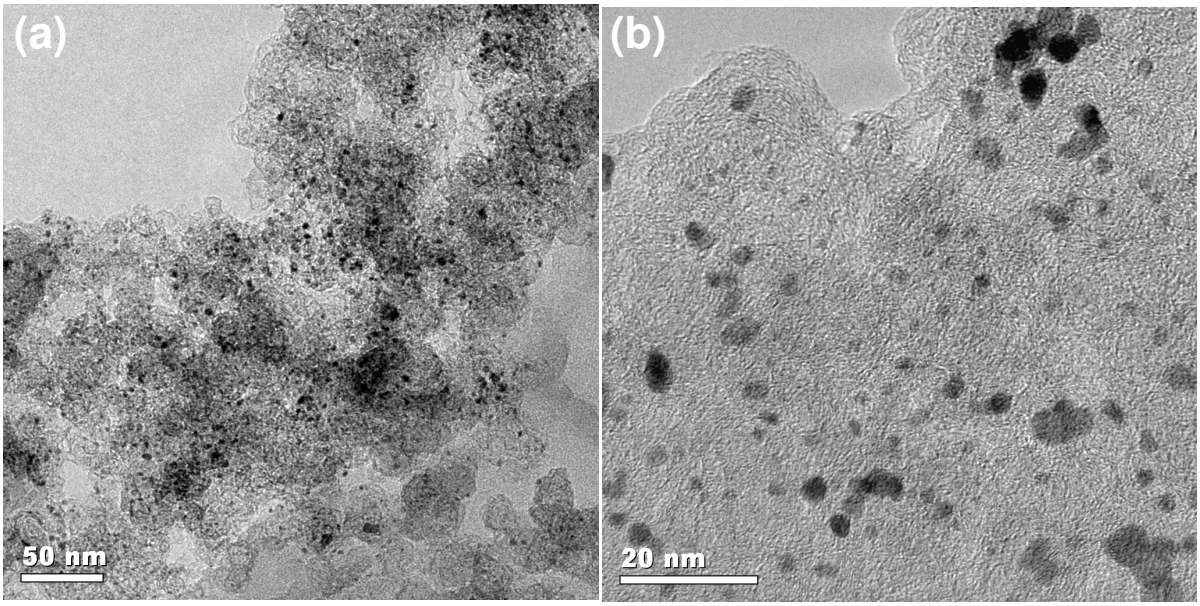


**Figure 4.14:** TEM image of the Pt/BP 2000 particles.

## 4.4 Preparation and characterization of Pt-Pd/BP 2000

In order to prepare bimetallic Pt-Pd/BP 2000 catalysts, two different methods were followed. The first is the common method consisting in the deposition of the nonprecious metal (Pd) on a previously formed carbon-supported Pt. This method involved dissolution and adsorption of the first organometallic precursor, $PtMe_2COD$ onto BP 2000 in $scCO_2$ at 20 MPa and 60 $^0$C . In order to convert the adsorbed $PtMe_2COD$ into Pt particles, reduction at atmospheric pressure under flow of $H_2/N_2$ at 200 $^0$C was carried out. Then, the second

organometallic precursor, $Pd(acac)_2$ was impregnated onto the previously prepared Pt/BP 2000 in $scCO_2$ at 20 MPa and 80 $^0$C. Reduction of $Pd(acac)_2$ molecules was completed in $H_2/scCO_2$ ($P_{H2}$= 0.8 MPa, $P_{TOT}$= 27.6 MPa) at 80 $^0$C. The summary of the preparation procedure and results from method 1 are given in Table 4.5. It can be seen that an increase in Pt metal loading did not influence the Pt average particle size for Pt/BP 2000 catalysts; whereas addition and increase of Pd content increased the Pt-Pd bimetallic particle size for the Pt-Pd/BP 2000 catalysts. In this method, introduction of the second metal leads to enlarge the average size of the bimetallic nanoparticles. The larger size can perhaps be attributed to one possible reason that the two step chemical reduction would generate core-shell (Pt-Pd) crystalline structures. It can be presumably due to the fact that Pd particles may cover Pt particles, thus slightly increasing the bimetallic particle size. The XRD patterns of the Pt-Pd/BP 2000 catalysts prepared by method 1 is given in Figure 4.15.

**Table 4.5:** The summary of the preparation and results for the Pt-Pd/BP 2000 catalysts prepared by method 1.

| | **Adsorption and reduction details** | **Pt-Pd/BP 2000 samples** | | |
|---|---|---|---|---|
| | | **1** | **2** | **3** |
| **STEP 1** | **Substrate amount (mg)** | 100 | 100 | 100 |
| | **Pt $Me_2$COD amount (mg)** | 51.3 | 25 | 60 |
| | **Adsorption experiment conditions;P(MPa), T ($^0$C)** | 20 MPa, 60 $^0$C | 20 MPa, 60 $^0$C | 20 MPa, 60 $^0$C |
| | **Adsorbed Pt$Me_2$COD amount** | 37.5 | 23 | 43 |
| | **Reduction method for Pt$Me_2$COD/BP 2000** | At atmospheric pressure under $H_2/N_2$ at 200 $^0$C for 4 hours | At atmospheric pressure under $H_2/N_2$ at 200 $^0$C for 4 hours | At atmospheric pressure under $H_2/N_2$ at 200 $^0$C for 4 hours |
| | **Pt loading (mg)** | 22 | 13.4 | 23 |
| | **XRD average particle size of Pt (nm)** | 2 | 2 | 2 |
| **STEP 2** | **Pt + BP 2000 amount of Pt/BP 2000 composites before step 2** | 14.8 mg Pt + 68 mg BP 2000 | 6.98 mg Pt + 64.82 mg BP 2000 | 19.1 mg Pt + 79 mg BP 2000 |
| | **Pd$(acac)_2$ amount (mg)** | 50. 5 | 60.6 | 20 |
| | **Adsorption experiment conditions** | 20 MPa, 80 $^0$C | 20 MPa, 80 $^0$C | 20 MPa, 80 $^0$C |
| | **Reduction method for Pt-Pd$(acac)_2$/BP 2000** | Chemical reduction in $H_2/scCO_2$ ($P_{H2}$= 0.8 MPa, $P_{TOT}$= 27.6 MPa) at 80 $^0$C for 6 hours | Chemical reduction in $H_2/scCO_2$ ($P_{H2}$= 0.8 MPa, $P_{TOT}$= 27.6 MPa) at 80 $^0$C for 6 hours | Chemical reduction in $H_2/scCO_2$ ($P_{H2}$= 0.8 MPa, $P_{TOT}$= 27.6 MPa) at 80 $^0$C for 6 hours |
| | **Pd loading (mg)** | 17.4 | 15 | 6 |
| | **Pt:Pd molar ratio** | (1:2) | (1:4) | (2:1) |
| | **XRD average particle size of Pt-Pd (nm)** | 3.91 | 5.104 | 3.2 |

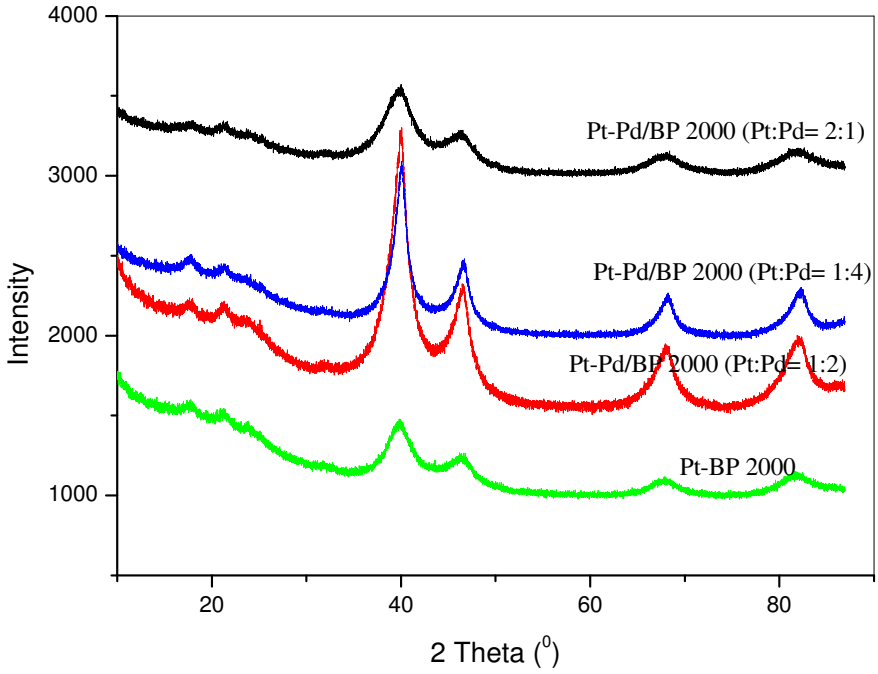


**Figure 4.15:** The XRD patterns of the Pt-Pd/BP 2000 catalysts with different Pt:Pd ratios prepared by method 1.

The average XRD particle sizes of the supported Pt-Pd bimetallic nanoparticles prepared by method 1 increase as the Pd content increases. The increase in average XRD particle size of the bimetallic catalysts with respect to Pd:Pt molar ratio is given in Figure 4.16.

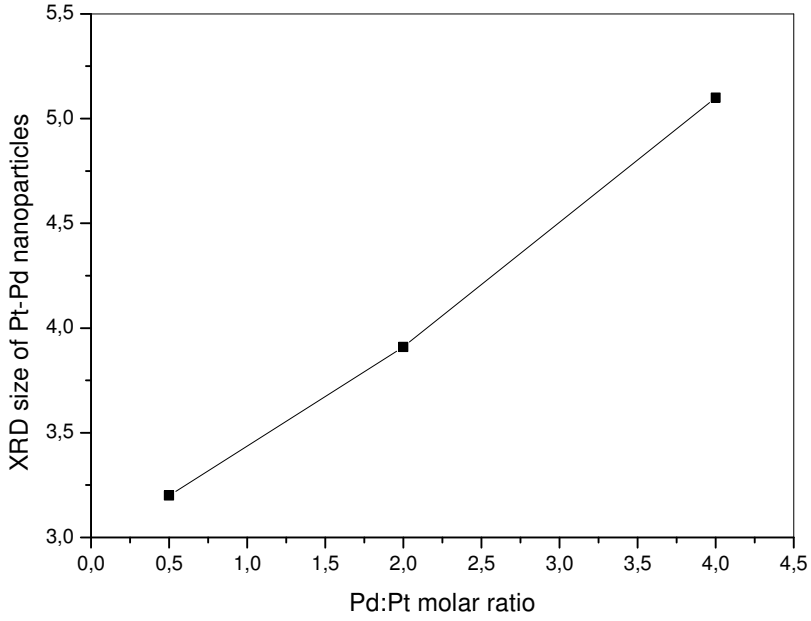


**Figure 4.16:** The XRD particle size of Pt-Pd/BP 2000 catalysts prepared by method 1 with respect to Pd:Pt molar ratio.

Utilizing the second method, 16 wt.% metal loaded Pd-Pt/BP2000 binary metallic nanoparticles were obtained first by simultaneous adsorption of a certain amount of $Pd(acac)_2$ and $PtMe_2COD$ from $scCO_2$ at 20 MPa and 80 $^0$C onto the surface of BP2000. Subsequently, the precursors were reduced concurrently in a $H_2/scCO_2$ mixture at 27.6 MPa ($P_{H2}$= 0.8 MPa) and 80 $^0$C. The molar ratio of Pt:Pd was 0.92 in the prepared catalysts and these showed much better control of nanoparticle size than in the Pd/BP2000 catalysts. Compared to method 1 for the preparation of supported bimetallic Pt-Pd catalysts, this method leads to the direct formation of Pt-Pd crystallites whereas Pt-Pd bimetallic nanoparticles formation occurs via the diffusion of Pd atoms in the Pt lattice with the first method. The XRD spectrum obtained from the Pd-Pt/BP2000 sample is presented in Figure 4.17 along with the corresponding XRD spectra from the Pd/BP2000 and Pt/BP2000

samples for comparison. The average metal particle size of the Pd-Pt/BP2000 catalyst calculated from the XRD spectrum using Scherrer formula is 9 nm.

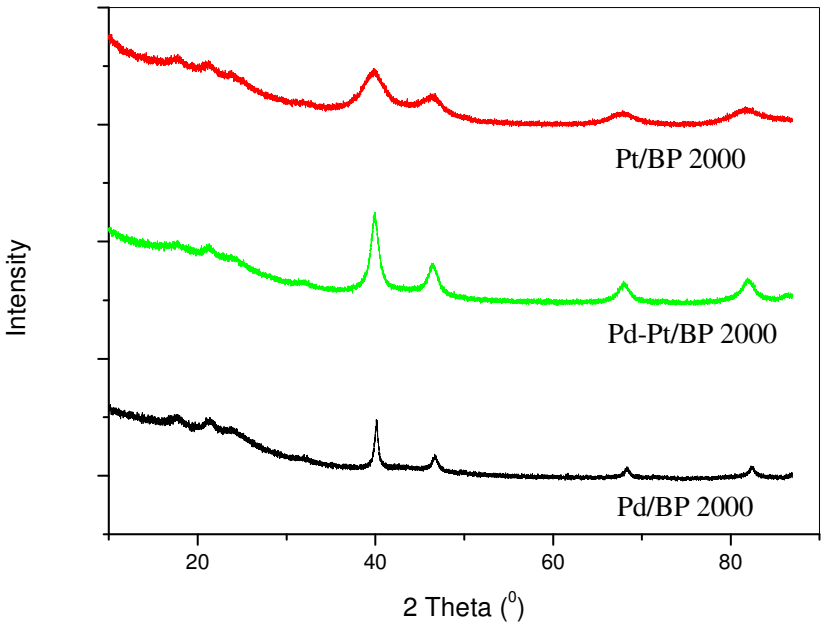


**Figure 4.17:** XRD spectrum for Pd-Pt/BP2000 catalyst with 0.92 Pt:Pd molar ratio prepared by method 2.

TEM images shown in Figure 4.18 obtained from the Pd-Pt/BP2000 catalyst samples show metal nano-particles that are distributed more homogeneously than those in the Pd/BP2000 catalyst but less homogeneously than those in the Pt/BP2000 catalyst. Similarly, the particle size distributions are narrower than those for the Pd/BP2000 catalyst but broader than those for the Pt/BP2000 catalyst, with the diameters for most of the particles lying between 2 and 10 nm.

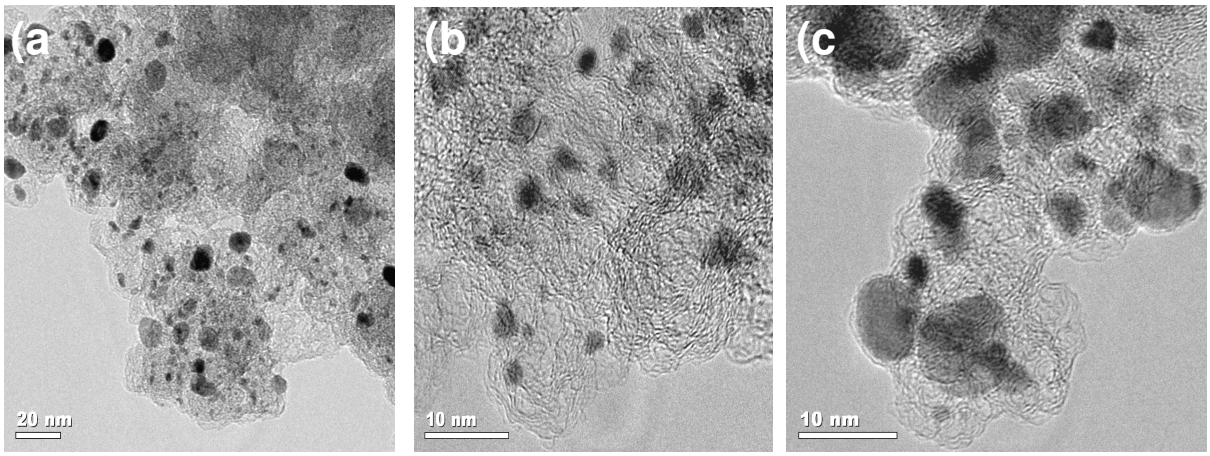


**Figure 4.18:** TEM images of the Pt-Pd/BP2000 with Pt:Pd molar ratio of 0.92 utilizing method 2.

Attempts to measure the chemistry of these particles by EDS were complicated by the high particle density in these bimetallic catalysts, which meant that spectra acquired from a particular particle included contributions from adjacent particles. Despite this, a comparison of many such spectra from regions that contain predominantly larger or smaller particles (e.g. areas such as those shown in Figures 4.18: (a) and 4.18: (b), respectively) revealed that the smaller particles are less Pd-rich than the larger particles. The EDS results for the prepared 0.92 Pt:Pd molar ratio utilizing method 2 is given in Figure 4.19. As can be seen from this figure, bimetallic nanoparticles rich in Pt content with 54.5 wt.% Pt and 45.5 wt.% Pd had small particle sizes between 3-5 nm; whereas size of the bimetallic nanoparticles rich in Pd content with 61.6 wt.% Pd and 38.4 wt.% Pt increased to 10 nm.

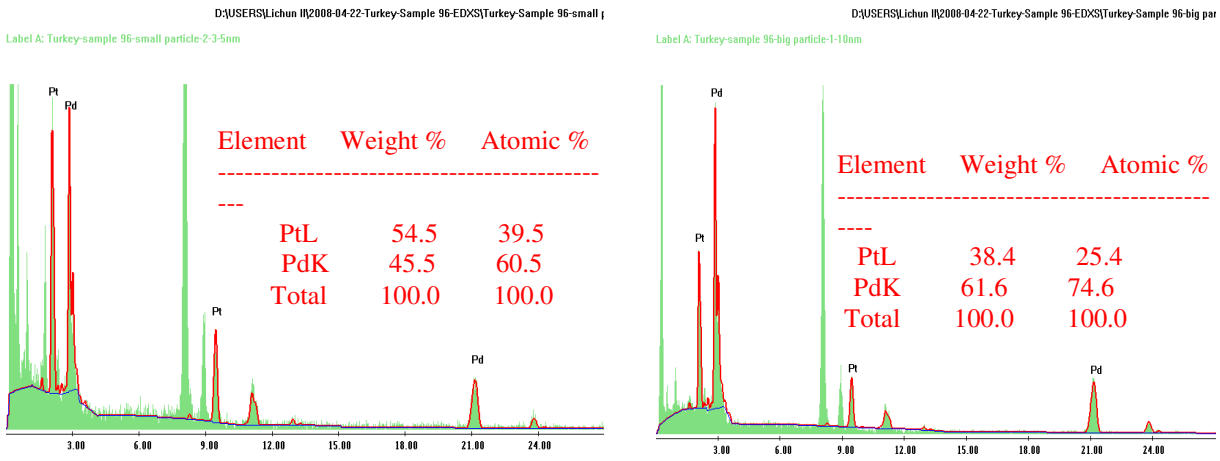


**Figure 4.19:** EDS weight compositions of the Pt-Pd/BP 2000 with Pt:Pd molar ratio of 0.92 prepared by reduction of the OMs of both metals adsorbed on the surface of BP 2000 in H2/scCO2 at 80 0C, simulatenously. (a) Small particles between 3-5 nm. (b) Big particles ~10 nm.

# 5 SUMMARY & FUTURE RESEARCH WORK

The $scCO_2$ deposition technique was used to prepare BP2000 supported single Pd, Pt and bimetallic Pd-Pt nanoparticles. The organometallics used for the study were $Pd(acac)_2$ and $PtMe_2COD$. In order to understand the correlation between the concentration of the OMs in the supercritical phase and the uptake amount of the OMs on the substrate at the given experimental conditions of 20 MPa and 60 $^0$C, the adsorption isotherms were measured for the $Pd(acac)_2$ and $PtMe_2COD$ on BP2000 in $scCO_2$. It was shown that the adsorption isotherm for $Pd(acac)_2$-BP2000-$scCO_2$ system was linear which was attributed to the low solubility of $Pd(acac)_2$ in $scCO_2$ at the given experimental conditions. The adsorption isotherm of the $PtMe_2COD$ on BP2000 in $scCO_2$ at 20 MPa and 60 $^0$C was represented by Langmuir model. The uptake amount of $Pd(acac)_2$ on the support was higher than the uptake amount of $PtMe_2COD$ at the same fluid concentration in the supercritical phase indicative of a stronger precursor-support interaction for $Pd(acac)_2$-BP2000. The metal loadings of the supports could be thermodynamically controlled using the adsorption isotherms. A mass transfer model was found to describe the adsorption kinetics for the $Pd(acac)_2$-BP2000-$scCO_2$ system at 20 MPa and 60 $^0$C with a fitting error of 5.6 % to the experimental data. It was found that the Pd precursor could be reduced in a $H_2/scCO_2$ mixture. From the XRD data, it was found that increasing reduction temperature and Pd metal loading increased the Pd particle size. From the TEM images it was seen that Pd particles were not homogeneously distributed on the BP2000 support with numerous large particles with sizes ranging from 3-100 nm. In contrast to Pd nanoparticles, Pt particles were found to be homogeneously distributed with small particle sizes between 2-4 nm on BP2000. Binary metal nanoparticles of Pd-Pt on BP2000 could also be formed. Two different methods were utilized. The first is the common method consisting in the deposition of the nonprecious metal (Pd) on a previously formed carbon-supported Pt. In

this method it was found that introduction of the Pd increased the average size of the bimetallic nanoparticles. For different molar ratio catalysts prepared by this method, the XRD average sizes of the bimetallic nanoparticles were found to be 2 nm, 3.2 nm, 3.91 nm and 5.1 nm for the Pt/C $Pt_2Pd_1$/C, $Pt_1Pd_2$/C and $Pt_1Pd_4$, respectively. In the second method, there is simultaneous adsorption and subsequent reduction of the organometallic precursors in $H_2/scCO_2$ mixture. It was again found that addition of Pt increased the homogeneity and reduced the particle size on the support compared to single Pd nanoparticles. At the same experimental conditions, it was found that supported bimetallic Pt-Pd nanoparticle size was 9 nm whereas single Pd size was 14 nm from TEM and XRD data. When the two methods were compared it was seen that the catalysts prepared by method 1 were smaller in size compared to the ones prepared by method 2. From the EDS results, it was seen that the smaller particles were less Pd-rich than the larger particles.

For further stages of this research, deeper investigation about the preparation of bimetallic carbon supported Pt-Pd nanoparticles can be done. Binary adsorption isotherms of the $PtMe_2COD$ – $Pd(acac)_2$ – BP 2000 can be obtained at determined experimental conditions. With the help of these isotherms, the amount of the incorporated metal on the substrate can be estimated for the simultaneous adsorption and reduction mechanism in the preparation of supported bimetallic Pt-Pd nanoparticles. Phase diagrams and alloy formation can be studied. More experiments can be carried out in order to obtain the relation between the size and composition of the bimetallic nanoparticles. The lattice parameters and composition relationship depending on Vegard's law can be obtained. Depending on the size and composition of the bimetallic nanoparticles, studies for the optimization of reduction temperature in $H_2/scCO_2$ mixture can be carried out.

**BIBLIOGRAPHY**

[1] A.L. Dantas, P.D. Alves, D.Arando, M. Schmal, Characterization of carbon supported Pd catalysts: influence of electronic and particle size effects using reaction probes, Appl. Catal., 277 (2004), 71-81.

[2] H.Li, G.Sun, N.Li, S.Sun, D.Su, Q.Xin, Design and preparation of highly active Pt-Pd/C catalyst for the oxygen reduction reaction, J.Phys.Chem., 111 (2007), 5605-5617.

[3]M.Markus, M. Kumar, K. Eklund, H. Sjöholm, S. Munzin, Hydrogenolysis of hydroxymatairesol over carbon supported palladium catalysts, Catal. Letters, 1103 (2005) 125-131.

[4] J. Luo, P.N. Njoki, Y. Lin, D. Mott, L. Wang, C. Zhong, Characterization of carbon-supported AuPt nanoparticles for electrocatalytic methanol oxidation reaction, Langmuir 22 (2006), 2892-2898.

[5] L. Xiong, A. Manthiram, Electrochim. Acta, 50 (2005), 2323.

[6] E. Antolini, J.R.C.Salgado, L.G.R.A. Santos, G. Garcia, E.A. Ticianelli, E. Pastor, E.R. Gonzalez, Carbon supported Pt-Cr alloys as oxygen-reduction catalysts for direct methanol fuel cells, Journal of Applied Electrochemistry, 36 (2005), 355-362.

[7] C.A. Angelucci, M. Silva, F.C. Nart, Preparation of platinum-ruthenium alloys supported on carbon by a sonochemical method, Electochemica **52** (2007) 7293-7299.

[8] W.Wang, D.Zheng, C. Du, Z.Zou, X.Zhang, B.Xia, H.Yang, D.Akins, Carbon supported Pd-Co bimetallic nanoparticles as electrocatalysts for the oxygen reduction reaction, J. Power Sources, 167 (2007), 243-249.

[9] G. Ren, H.Shi, Y.Xing, Synthesis and composition evolution of bimetallic Pd-Pt alloy nanoparticles, IOP electronic journals-Nanotechnology, 18 (2007).

[10] C.D. Saquing, T.T. Cheng, M. Aindow, C.Erkey, Preparation of Platinum/Carbon Aerogel Nanocomposites Using a Supercritical Deposition Method, J.Phys.Chem.B., 108 (2004), 7716-7722.

[11] C.D.Saquing, D.Kang, M. Aindow, C.Erkey, Investigation of the Supercritical Deposition of Platinum Nanoparticles into Carbon Aerogels, Microporous and Mesoporous Materials, 80 (2005), 11-23.

[12] A. Bayrakceken, U. Kitkamthorn, M. Aindow, C. Erkey, Decoration of multi-walled carbon nanotubes with platinum nanoparticles using supercritical deposition with thermodynamic control of metal loading, Scripta Materialia, 56 (2007), 101-103.

[13] A. Bayrakçeken, A.Smirnova, U. Kitkamthorn, M. Aindow, L. Türker, İ.Eroğlu, C. Erkey, Pt-based electrocatalysts for polymer electrolyte membrane fuel cells prepared by supercritical deposition technique, J. Power Sources, 179 (2008), 532-540.

[14]Y.Zhang, D.Kang, M.Aindow, C.Erkey, Preparation and characterization of Ruthenium/Carbon Aerogel nanocomposites via a supercritical fluid route, J.Phys.Chem. B., 109 (2005), 2617-2624.

[15] Y.Zhang, C. Erkey, Preparation of supported metallic nanoparticles using supercritical fluids: A review, J.Supercrit. Fluids, 38 (2006), 252-267.

[16] X.R. Ye, Y. Lin, C.M. Wai, Decorating catalytic palladium nanoparticles on carbon nanotubes in supercritical carbon dioxide, Chem. Commun., 5 (2003), 642.

[17] X.R.Ye, Y. Lin, C. Wang, M.H.Engelhard, Y.Wang, C.M.Wai, Supercritical fluid synthesis and characterization of catalytic metal nanoparticles on carbon nanotubes, Journal of Materials Chemistry, 14 (2004), 908-913.

[18] M.Kruk, M. Jaroniec, Y. Bereznitski, Adsorption study of porous structure development in carbon blacks, J. Colloid and Interface Science, 182 (1996), 282-288.

[19] Y. Zhang, B. Cangul, Y. Garrabos and C. Erkey, Thermodynamics and kinetics of adsorption of bis(2,2,6,6-tetramethyl-3,5-heptanedionato) (1,5-cyclooctadiene) ruthenium (II), J. Supercrit. Fluids, 44 (2008), 77.

[20] S.R., Puniredd, S. Weiyi, M.P. Srnivasan, Pd-Pt and Fe-Ni nanoparticles formed by covalent molecular assembly in supercritical carbon dioxide, Journal of Colloidal and Interface Science, 320 (2008), 333-340.

[21] E. Antolini, J.R.C. Salgado, R.M. Silva, E.R. Gonzalez, Preparation of carbon supported binary Pt-M alloy catalysts (M: first row transition metals) by low/medium temperature methods, Materials Chemistry and Physics, 101 (2007), 395-403.

[22] E. Antolini, Formation of carbon-supported PtM alloys for low temperature fuel cells: a review, Materials Chemistry and Physics, 78 (2003), 563-573.

[23] www.electrochem.org/meetings/scheduler/abstracts/214/0845.pdf

[24] B. Pawelec, L. Parola, R.M. Navarro, S. Murcia-Mascaros, J.L.G. Fierro, On the origin of the high performance of MWNT-supported PtPd catalysts fort he hydrogenation of aromatics, Carbon, 44 (2006), 84-98.

[25] H. Li, G. Sun, N. Li, S. Sun, D. Su, Q. Xin, Design and Preparation of Highly Active Pt-Pd/C Catalyst fort he Oxygen Reduction Reaction, J.Phys.Chem. C, 111 (2007), 5605-5617.

[26] P.L. Hanson, A.M. Molenbroek, A.V. Ruban, Alloy Formation and Surface Segregation in Zeolite Supported Pt-Pd Bimetallic Catalysts, J.Phys.Chem.B, 101 (1997), 1861-1868.

[27] A. Morlang, U. Neuhausen, K.V. Klementiev, F.W. Schütze, G. Miehe, H. Fuess, E.S. Lox, Bimetallic Pt/Pd Diesel Oxidation Catalysts Structural Characterization and Catalytic Behavior, Applied Catalysis B: Environmental, 60 (2005), 191-199.

[28] D. William, Jr. Callister, Materials Science & Engineering An Introduction, 6 th edition, John Wiley & Sons, (2003) 250-253.

[29]M. Hillert, Phase equilibria, phase diagrams and phase transformations: their thermodynamic basis, New York: Cambridge University Pres, (1998).

[30] C.W. Hills, N.H. Mack, R.G. Nuzzo, The Size-Dependent Structural Phase Behaviors of Supported Bimetallic (Pt-Ru) Nanoparticles, J.Phys. Chem. B., 107 (2003), 2626-2636.

[31] M.S. Nashner, A.I. Frenkel, D.A. Adler, J.R. Shapley, R.G. Nuzzo, J.Am.Chem.Soc., 119 (1997), 7760.

[32] Z. Peng, H. Yang, Ag-Pt alloy nanoparticles with the compositions in the miscibility gap, Journal of Solid State Chemistry, 181 (2008), 1546-1551.

[33]F. Cansel, C. Aymonier, A. Loppiner-Serani, Review on materials science and supercritical fluids, Current Opininon in Solid State and Materials Science, **7** (2003), 331-340.

[34]C. Aymonier, A. Loppiner-Serani, H. Reveron, Y. Garrabos, F. Cansel, Review of supercritical fluids in inorganic materials science, J.of Supercritical fluids, 38 (2006) 242-251.

[35] F. Cansel, B. Chevalier, A. Demourgues, J. Etourneau, C. Even, Y. Garrabos, V. Pessey, S. Petit, A. Tressaud, F. Weill, Supercritical fluid processing: a new route for materials synthesis, Journal of Materials Chemistry, 9 (1999), 67-75.

[36] B. Zhao, T. Momose, Y. Shimogaki, Deposition of Cu-Ag Alloy Film by Supercritical deposition, Japanese Journal of Applied Physics, 45 (2006), 1296-1299.

[37] Papers presented at a symposium held June 23-24, 1989, sponsored by the Institute of Food Technologists and the International Union of Food Science and Technology.

[38] J.A. Darr, M. Poliakoff, New Directions in Inorganic and Metal-Organic Coordination Chemistry in Supercritical Fluids, Chem.Rev., 99 (1999), 495-541.

[39] O. Aschenbrenner, S. Kemper, N. Dahmen, K. Schaber, E. Dinjus, Solubility of ß-diketonates, cyclopentadienyls, and cyclooctadiene complexes with various metals in supercritical carbon dioxide, Jour.of.Supercritical fluids, 41 (2007), 179-186.

[40] A.F. Lagalante, B.N. Hansen, T.J. Bruno, Solubilities of copper (II) and chromium (III) β-diketonates in supercritical carbon dioxide, Inorg.Chem., 34 (1995), 5781-5785.

[41] A.V. Yazdi, E.J. Beckman, Design, Synthesis, and Evaluation of Novel, Highly $CO_2$-Soluble Chelating Agents for Removal of Metals., Ind. Eng. Chem. Res., 35 (1996), 3644.

[42] C. Burda, X. Chen, R. Narayanan, M. El-Sayed, Chemistry and Properties of Nanocrystals of Different Shapes, Chem.Rev., 105 (2005), 1025-1102.

[43] B. Wong, S. Yoda, S.M. Howdle, The preparation of gold nanoparticle composites using supercritical carbon dioxide, J.of Supercritical Fluids, 42 (2007), 282-287.

[44] S. Moisan, V. Martinez, P. Weisbecker, F. Cansel, S. Mecking, C. Aymonier, General Approach for the synthesis of Organic-Inorganic Hybrid Nanoparticles Mediated by Supercritical $CO_2$, J.Am.Chem.Soc., 129 (2007), 10602-10606.

[45] C.H. Yen, K. Shimizu, Y. Lin, F. Bailey, I.F. Cheng, C.M. Wai, Chemical Fluid Deposition of Pt-Based Bimetallic Nanoparticles on Multiwalled Carbon Nanotubes for Direct Methanol Fuel Cell Application, Energy & Fuels, 21 (2007), 2268-2271.

[46] http://en.wikipedia.org/wiki/Energy_dispersive_X-ray_spectroscopy

[47] http://www.thermo.com/com/cda/technology/detail/1,,12700,00.html.

[48] Fogler, H.Scott, Elements of Chemical Reaction Engineering, 3rd edition, Prentice-Hall International Inc., New Jersey, (1999), 739-741.

[49] J.M. Smith, Chemical Engineering Kinetics, second ed., McGraw-Hill, Tokyo, (1970), 317, 465.

[50] D. Jayne, Y. Zhang, S. Haji, C. Erkey, Dynamics for removal of organosulfur compounds from diesel by adsorption on carbon aerogels for fuel cell applications, International Journal of Hydrogen Energy, 30 (2005), 1287-1293.

[51] M. Kruk, M., Jaroniec, Y. Bereznitski, Adsorption study of porous structure development in carbon blacks, Jour.of Colloid and Interface Science, 182 (1996), 282-288.

[52] T. Funazukuri, C.Y. Kong, S. Kagei, Impulse response techniques to measure binary diffusion coefficients under supercritical conditions, J.Chromatogr. A. 1037 (2004), 411-429.

[53] R.B. Bird, W.E. Stewart, E.N. Lightfoot, Transport Phenomena, 2nd edition, John Wiley & Sons (2002), 864.

[54] J. Kim, G. Roberts, D.J. Kiserow, Supported Pd Catalyst Preparation Using Liquid Carbon Dioxide, Chem.Mater., 18 (2006), 4710-1712.

## VITA

Betül Cangül was born in Bursa, Turkey in 1984. She graduated from Middle East Technical University (METU), Ankara, Turkey in 2006 where she he held her B.Sc. degree in Chemical Engineering. After graduation, she was accepted from Materials Science and Engineering Department of Koç University, Istanbul, Turkey for graduate studies. During her M.Sc. studies she worked on preparation of carbon supported Pd, Pt and bimetallic Pt-Pd nanoparticles by sc$CO_2$ deposition under the supervision of Professor Can Erkey. In her graduate studies, she also worked as a teaching assistant for Process & Product Design and Chemical & Biological Engineering Laboratory courses.

Following her M.Sc. studies, she is pursuing a career in the Quality Direction of Oyak Renault, Turkey as a supplier quality engineer.